Whole Atmosphere Community Climate Model — eXtended Version 2.0 Scientific Description

Han-Li Liu[1], Charles G. Bardeen[2], Benjamin T. Foster[1], Peter Lauritzen[3], Jing Liu[1], Gang Lu[1], Daniel R. Marsh[1,2], Astrid Maute[1], Joseph M. McInerney[1], Nicholas M. Pedatella[1], Liying Qian[1], Arthur D. Richmond[1], Raymond G. Roble[1], Stanley C. Solomon[1], Francis M. Vitt[1,2], Wenbin Wang[1]

[1]High Altitude Observatory, National Center for Atmospheric Research, Boulder, Colorado, USA
[2]Atmospheric Chemistry Observations and Modeling, National Center for Atmospheric Research, Boulder, Colorado, USA
[3]Climate and Global Dynamics, National Center for Atmospheric Research, Boulder, Colorado, USA

Abstract

Key developments have been made to the NCAR Whole Atmosphere Community Climate Model with thermosphere and ionosphere extension (WACCM-X). Among them the most important are the self-consistent solution of global electrodynamics, and transport of O^+ in the F-region. Other ionosphere developments include time-dependent solution of electron/ion temperatures, metastable O^+ chemistry, and high-cadence solar EUV capability. Additional developments of the thermospheric components are improvements to the momentum and energy equation solvers to account for variable mean molecular mass and specific heat, a new divergence damping scheme, and cooling by $O(^3P)$ fine structure. Simulations using this new version of WACCM-X (2.0) have been carried out for solar maximum and minimum conditions. Thermospheric composition, density, and temperatures are in general agreement with measurements and empirical models, including the equatorial mass density anomaly and the midnight density maximum. The amplitudes and seasonal variations of atmospheric tides in the mesosphere and lower thermosphere are in good agreement with observations. Although global mean thermospheric densities are comparable with observations of the annual variation, they lack a clear semi-annual variation. In the ionosphere, the low-latitude E×B drifts agree well with observations in their magnitudes, local time dependence, seasonal, and solar activity variations. The pre-reversal enhancement in the equatorial region, which is associated with ionospheric irregularities, displays patterns of longitudinal and seasonal variation that are similar to observations. Ionospheric density from the model simulations reproduces the equatorial ionosphere anomaly structures, and is in general agreement with observations. The model simulations also capture important ionospheric features during storms.

This document is extracted in part from the paper by H.-L. Liu et al. in the *Journal of Advances in Modeling Earth Systems*, *10*, 381, doi:10.1002/2017MS001232, 2018. The paper by Liu et al., which includes initial validation comparisons, can also be found in the WACCM-X documentation directory. This document also contains appendices providing more detail concerning the electrodynamics and O^+ transport calculations, which were taken from TIE-GCM documentation compiled by A. Maute et al.

1 Introduction

The terrestrial ionosphere exhibits variability on timescales ranging from minutes to diurnal, from days to solar rotations, and from solar cycles to centuries. These variations are primarily driven by manifestations of solar magnetism, including ultraviolet radiation, the solar wind, and the interplanetary magnetic field, which are processed by their interaction with the Earth's magnetosphere. Ionosphere density is a small fraction (10^{-3} to 10^{-6}) of the neutral atmosphere density, and it has long been recognized that the thermospheric response to solar variation is important in determining ionospheric changes, since the neutral and ionized gases form a strongly coupled system that cannot be meaningfully described in isolation. The thermosphere and ionosphere are integral parts of the whole atmosphere system, and more recent perspectives emphasize the importance of lower atmospheric dynamics and chemistry, including weather systems, gravity waves, planetary waves, tidal variations, seasonal cycles, and long-term climate change, in driving the variability of thermosphere-ionosphere system [e.g. *Liu and Roble*, 2002; *Immel et al.*, 2006; *Qian et al.*, 2009; *Goncharenko et al.*, 2010a,b; *Pedatella et al.*, 2012; *Solomon et al.*, 2015b; *Liu*, 2016].

Numerical modeling of the thermosphere-ionosphere system has historically been approached by specifying upper boundary conditions representing solar and magnetospheric processes, and lower boundary conditions representing climatological or parameterized forcing of atmospheric state variables at some interface, generally in the stratosphere-mesosphere region. For instance, the NCAR Thermosphere-Ionosphere-Electrodynamics General Circulation Model (TIE-GCM) [*Richmond et al.*, 1992; *Qian et al.*, 2014] and

Thermosphere-Ionosphere-Mesosphere-Electrodynamics General Circulation Model (TIME-GCM) [*Roble and Ridley*, 1994] have lower boundaries at 97 and 30 km, respectively; these lower boundary conditions are specified using tidal parameterizations or observed meteorological fields [e.g. *Hagan et al.*, 2007]. However, with the development of whole atmosphere models [e.g. *Marsh et al.*, 2007; *Akmaev*, 2011], there is an opportunity to adopt a fully-self-consistent numerical description of the entire atmosphere-ionosphere system. Early efforts to accomplish this are described in *Liu et al.* [2010]. In this paper, we describe new advances of the NCAR WACCM-X that now forms a comprehensive description of atmosphere-ionosphere interaction. The most important of these are the incorporation of a fully-coupled low and middle latitude electrodynamo, dynamical transport of the atomic oxygen ions, and high latitude forcing by the magnetospheric electric fields and auroral Joule and particle heating.

2 Thermosphere-Ionosphere Extension of the Whole Atmosphere Community Climate Model

WACCM-X is a configuration of the NCAR Community Earth System Model (CESM) [*Hurrell et al.*, 2013] that extends the atmospheric component into the thermosphere, with a model top boundary between 500–700 km. As a part of CESM, WACCM-X is uniquely capable of being run in a configuration where the atmosphere is coupled to active or prescribed ocean, sea ice, and land components, enabling studies of thermospheric and ionospheric weather and climate. Physical processes represented in WACCM-X build upon those in regular WACCM, which has a model top at ~130 km, and in turn is built upon the Community Atmosphere Model (CAM), which goes up to ~40 km. The physics of these models is described in *Marsh et al.* [2013] and *Neale et al.* [2013]. Recent revisons and improvements to WACCM, which are therefore included in WACCM-X, include:

1. Revision of parameterized non-orographic gravity wave forcing as described by *Richter et al.* [2010] and *Garcia et al.* [2017].
2. Introduction of surface stress due to unresolved topography that led to significant improvements in the frequency of stratospheric sudden warmings [*Richter et al.*, 2010; *Marsh et al.*, 2013].
3. Chemical kinetic and photochemical rate constants updated to the Jet Propulsion Laboratory recommendations [*Sander et al.*, 2011].
4. A new treatment of stratospheric heterogenous ozone loss [*Solomon et al.*, 2015a].
5. Protocols from the Chemistry Climate Model Initiative [*Eyring et al.*, 2013] are used for the specification of time-dependent greenhouse gases and ozone depleting substances.

In addition, two metastable O^+ states, $O^+(^2D)$ and $O^+(^2P)$, have been added to the chemistry package, which already includes 5 ions (O^+, O_2^+, NO^+, N^+, and N_2^+), electrons and 74 neutral species. The model has 87 photolysis and photo-ionization reactions and 202 gas phase and heterogeneous reactions. The specification of solar spectral irradiance at wavelengths from Lyman-α to the near infrared are unchanged from *Marsh et al.* [2013] and continues to use the empirical model of *Lean et al.* [2005]. EUV and X-ray fluxes implemented are described below.

At the standard model resolution, the model does not generate a quasi-biennial oscillation, but one can be imposed by relaxing the equatorial zonal winds in the stratosphere to the observed QBO zonal winds. Alternatively, for simulations of particular years in the recent historical record, WACCM-X has the option to constrain the tropospheric and stratospheric dynamics by reanalysis, namely, the 'specified-dynamics' or SD version of the model. This is currently done by relaxing temperature, zonal and meridional winds up to ~50km and surface pressure towards the Modern Era Retrospective Analysis for Research and Applications (MERRA).

WACCM-X is currently based on CAM-4 physics, as released in CESM 1.0, and employs a conventional latitude-longitude grid with horizontal resolution of 1.9° in latitude and 2.5° in longitude. Thus, it lags the incipient release of CESM 2.0, in which CAM and WACCM can be run at twice that resolution. The default vertical resolution is the same as WACCM below 0.96 hPa, but has been increased to one-quarter scale height above that pressure level. The model top pressure (p) is 4.1×10^{-10} hPa (typically between 500 to 700 km, depending on the solar and geomagnetic activity). Note that it is common practice to refer to log-pressure level as Z_p in units of scale height relative to a reference pressure, as is done in the TIE-GCM. The WACCM-X model top is equivalent to $Z_p = 7.1$, where $Z_p = ln(p_0/p)$ and $p_0 = 5 \times 10^{-7}$ hPa. It is about 28.5 scale heights above the Earth surface. A constant gravity acceleration (g), with the value at the Earth surface, is currently used in the model. It is thus necessary to rescale the model geopotential height, which is based on the constant g, according to gravitational law when analyzing model output. The model grid system does not consider the size differential of the upper and lower sides of grid cells, which may introduce errors on the order of z/r_e (z is the altitude and r_e is the Earth radius) for vertical flux quantities.

Earlier work, and the initial release of WACCM-X 1.0 [*Liu et al.*, 2010], included diffusive processes in the neutral thermosphere and a preliminary implementation of thermospheric neutral dynamics, using the CAM dynamical core, but did not include neutral wind dynamo, ionospheric transport, or calculation of ion/electron energetics and temperatures. WACCM-X 1.0, therefore, does not correctly resolve the thermospheric energetics or thermal structure. These processes, as well as many additional processes included in models such as the TIE-GCM have now been implemented in the new model. Compared with TIE-GCM and TIME-GCM, WACCM-X 2.0 has the advantage of self-consistently resolving lower atmospheric processes, and therefore enables more realistic simulation of upper atmospheric variability due to lower atmospheric forcing and better understanding and quantification of space weather and space climate. The model will be released as WACCM-X 2.0, and the following is a detailed description of the new developments.

2.1 Neutral Thermosphere Components

Although in the early version of WACCM-X species dependent specific heats and mean molecular weight (and along with it the gas constant of dry air) were taken into account in the physics modules [*Liu et al.*, 2010], these quantities were treated as constants in the finite volume (FV) dynamical core (often referred to as dycore). Changes have been made in the FV dycore to treat them properly (sections 2.1.1 and 2.1.3). Changes in divergence damping are described in section 2.1.2. Cooling of the neutral atmosphere by O(^{3}P) fine structure emission is now included in the model, as described in section 2.1.4.

2.1.1 Momentum equations

In the standard FV dycore, the vertical coordinate is based on Exner function p^κ (where κ is the ratio of gas constant of dry air R and specific heat at constant pressure c_p). Accordingly the pressure gradient calculation, using the contour integral method [*Lin*, 1997], uses the Exner function. When κ is a constant (below the homopause), a constant pressure surface translates to a surface with a constant Exner function, and the pressure gradient calculation is valid. However, this is no longer true when κ becomes a variable above the homopause: the control volume is distorted and the pressure gradient calculation is incorrect. This leads to excessively large mean meridional and vertical winds, and erroneous temperature structures in the thermosphere. This problem is solved by changing from Exner function based vertical coordinate to log-pressure vertical coordinate.

2.1.2 Divergence Damping

The FV discretization is designed to damp vorticity at grid scale [*Lin and Rood*, 1996, 1997], but an explicit scheme is needed to damp divergence and avoid spurious accumulation of the divergent component of total kinetic energy. In earlier versions of CAM, WACCM and WACCM-X, the second order divergence damping was the default, with a damping coefficient, $r_e^2 \Delta\lambda\Delta\theta/128\Delta t$ (where $\Delta\lambda, \Delta\theta$, and Δt are longitude and latitude spacing, and time-step respectively), applied uniformly at all grid points, except at the top 3 levels, where it monotonically increases by about 4-fold. In our numerical experiments using WACCM-X, however, we found that the second order divergence damping with the default damping coefficient is responsible for damping atmospheric tidal waves. By reducing the damping coefficient, the tidal amplitudes become much stronger than previously reported [*Liu et al.*, 2010], and are comparable with observations. In more recent versions of the FV dycore, a 4th order divergence damping has been introduced [*Lauritzen et al.*, 2012]. It has the advantage of more selectively damping out small-scale waves, while minimally impact planetary-scale waves. This is now the default option for WACCM-X.

2.1.3 Energy Equation and Hydrostatic Equation

The formulation of the energy equation of the neutral atmosphere in the standard FV dycore is based on potential temperature (Θ). Potential temperature, however, is not a well defined quantity in the thermosphere, where the mixing ratios of the major species are variables: when adiabatically moved to a reference level, the composition of an air parcel is likely to be different from that of the reference level atmosphere. This problem can be avoided if the energy equation is formulated based on temperature. It is also possible to work with the current FV formulation, by taking into account the κ variability when solving for potential temperature:

$$\frac{\partial \Theta \delta p}{\partial t} + \nabla_H \cdot (\mathbf{V_H} \Theta \delta p) = \Theta \ln(p/p_0)(\frac{\partial \kappa \delta p}{\partial t} + \nabla_H \cdot (\mathbf{V_H} \kappa \delta p)) \tag{1}$$

where δp is the layer thickness, ∇_H the horizontal divergence, and $\mathbf{V_H}$ the horizontal wind vector. It is noted that the correction term on the right hand side of Equation 1 is actually in the form of the advection of κ. Therefore, it is convenient to implement this correction term by treating κ as a tracer species. It is found that without this correction, spurious waves could be excited that become very large in the upper thermosphere, ultimately rendering the model unstable.

In the FV dycore, the following form of the hydrostatic equation, also based on potential temperature, is used to calculate geopotential Φ_{gp}: $\delta\Phi_{gp} = c_p \Theta \delta(p^\kappa)$. This relationship is incorrect with κ being a variable. The correct form

$$\delta\Phi_{gp} = c_p \kappa p^\kappa \Theta \delta(\ln(p)) \tag{2}$$

is used instead.

2.1.4 Cooling by O(^{3}P) Fine Structure Emission

The primary radiative cooling mechanisms for the thermosphere are excitation of CO_2 and NO by collisions with atomic oxygen, followed by infrared emission. These were included in the first version of WACCM-X. However, in the upper thermosphere, fine structure emission by O(^{3}P) at 63 μm is also important. This is calculated based on the local thermodynamic equilibrium (LTE) expression in *Bates* [1951] for the O(^{3}P) cooling rate $L_{O(^3P)}$ in erg g^{-1} s^{-1}:

$$L_{O(^3P)} = 0.835 \times 10^{-18} \frac{n([O])}{\rho} X_{fac} \frac{\exp(-228/T)}{1 + 0.6\exp(-228/T) + 0.2\exp(-325/T)} \tag{3}$$

where n([O]) is the atomic oxygen number density (in cm^{-3}), ρ is the total mass density (in g cm^{-3}), T is the neutral temperature (in Kelvin). X_{fac} is a masking factor for radiative transfer in an optically thick medium, based on *Kockarts and Peetermans* [1970]. This mechanism is included in WACCM-X 2.0, providing about -50 K temperature reduction at high altitudes, thus offsetting to some extent the additional heating generated by inclusion of O^+ metastables (see below).

2.2 Ionospheric Components

The new ionospheric component in WACCM-X includes modules of the ionospheric wind dynamo, F-region O^+ transport, and electron and ion temperatures, which are used to calculate heating of the neutral atmosphere through collisions with thermal electrons and ions. Also, two metastable O^+ states, $O^+(^2D)$ and $O^+(^2P)$, have been added to the WACCM-X chemistry package.

2.2.1 Electrodynamics

The ionospheric electrodynamics in WACCM-X are adapted from the TIE-GCM with the general aspects of modeling ionospheric electrodynamics discussed in *Richmond and Maute* [2014] and the specific details about TIE-GCM 2.0 electrodynamics given in *Maute* [2017]. In the following we describe in general terms the WACCM-X electrodynamics and point out differences with respect to the TIE-GCM electrodynamics.

In the thermosphere, ion-neutral coupling becomes important, and, through ion drag, neutral dynamics are influenced by the plasma motion and its associated electric field. Ion drag calculation is already included in WACCM-X 1.0, but the ion drifts are specified empirically. WACCM-X 2.0 electrodynamics calculate self-consistently electric fields and thus ion drifts at low and middle latitude, driven by the neutral wind dynamo. At high latitudes, the electric potential is imposed by an empirical model. Smaller forcing terms due to gravity and plasma pressure gradient driven current are neglected. Ionospheric electrodynamics in WACCM-X are treated as steady-state, with an electrostatic electric field E expressed by an electrostatic potential Φ through $E = -\nabla\Phi$. The ionospheric conductivities are highly anisotropic, with conductivities along the geomagnetic field lines several orders of magnitude larger than those perpendicular to the geomagnetic field. Therefore, on the spatial and temporal scales considered in WACCM-X, the geomagnetic field lines at middle and low latitude are considered equipotential at conjugate points.

The electrodynamics are formulated in a modified magnetic apex coordinate system [*Richmond*, 1995] using a realistic geomagnetic main field which is updated once per year based on the International Geomagnetic Reference Field (IGRF) [*Thébault et al.*, 2015]. The resulting partial differential equation is solved for the electric potential Φ given by equation (5.23) of *Richmond* [1995] using the field-line integrated quantities in equations (5.11)-(5.29) of *Richmond* [1995]. The ionospheric conductivities below ~80 km are assumed to be negligible, so the bottom boundary of the field line integration is set to a pressure level of 1.0 Pa, which is equivalent to ~80 km. The reference height at which the electric potential is determined is also set to 80 km. The spatial resolution of the ionospheric electrodynamics in WACCM-X is the same as in the TIE-GCM, 4.5° in magnetic longitude, and varying from 0.34° to 3.07° in magnetic latitude from the equator to the poles. Coordinate transform routines from the Earth System Modeling Framework (ESMF) are employed for mapping between the geographic and geomagnetic coordinate systems.

The electrodynamics solver obtains the global electric potential due to the wind dynamo at low and middle latitudes, with a high-latitude boundary condition prescribed by empirical electric potential patterns to simulate magnetospheric forcing. In the current version of WACCM-X, the empirical ion convection patterns are from *Heelis et al.* [1982] (see section 2.2.5). The wind dynamo is merged with the high latitude prescribed electric

potential between 60°–75° magnetic latitude, which allows the high-latitude potential to influence the low-latitude electrodynamo, approximating the effect of a penetration electric field.

Further detail concerning the electroynamo formulation is given in Appendix A. This description is derived from TIE-GCM documentation, and subroutine and variable names, etc., may differ from the WACCM-X implementation.

2.2.2 O^+ transport

Ion transport in WACCM-X 2.0 is calculated using the approximation that O^+ in the (^{4}S) ground state is the only ion that has a long enough lifetime to be subject to significant transport. Molecular ions have lifetimes that are short compared to the chemistry time-step of five minutes (except in the lower E-region, where transport is a minor consideration, and below 200 km at night, when the ion densities are so low they have little influence on the thermosphere). The light atomic ions H^+ and He^+, and metallic ions, are not yet included in the model. The excited metastable states of O^+ (see below) also have short lifetimes, and N^+ is considered a sufficiently minor species that any F-region transport will remain in chemical equilibrium with O^+.

The basic method is that O^+ transport is calculated separately from chemical production and loss (which is part of the interactive chemistry module), and the electron density is then adjusted to preserve charge neutrality. The dynamical solution is adapted from the TIE-GCM method described by *Roble et al.* [1988], and is summarized as follows.

The equation

$$\frac{\partial n_i}{\partial t} = -\nabla \cdot (n_i \mathbf{V_i}) \tag{4}$$

describes the transport of O^+, in terms of its number density n_i, by field-aligned plasma ambipolar diffusion, $E \times B$ drifts perpendicular to the magnetic field lines, and neutral winds along the magnetic field lines, where ion velocity $\mathbf{V_i}$ is defined as

$$\mathbf{V_i} = \mathbf{V}_\parallel + \mathbf{V}_\perp \tag{5a}$$

$$\mathbf{V}_\parallel = (\mathbf{b} \cdot \frac{1}{\nu_{in}}[\mathbf{g} - \frac{1}{\rho_i}\nabla(P_i + P_e)] + \mathbf{b} \cdot \mathbf{V})\mathbf{b} \tag{5b}$$

$$\mathbf{V}_\perp = \frac{\mathbf{E} \times \mathbf{B}}{|B|^2} \tag{5c}$$

where $\mathbf{V}_\parallel$ and $\mathbf{V}_\perp$ are the parallel and perpendicular ion velocities with respect to the geomagnetic field lines. The unit vector along the geomagnetic field line is $\mathbf{b}$, ν_{in} is the O^+ ion-neutral collision frequency, $\mathbf{g}$ is gravity, ρ_i is the O^+ mass density, P_i and P_e are the ion (O^+) and electron pressure, $\mathbf{V}$ is the neutral wind velocity, $|B|$ is the geomagnetic field strength, and $\mathbf{E}$ is the electric field. Note that Equation 5c neglects the influence of ion-neutral collisions on ion motion perpendicular to B; this influence is significant only in the E region where the O^+ lifetime is short and transport is unimportant.

Equation 4 is solved on the WACCM-X geographic latitude/longitude grid and pressure levels, using the finite difference method [*Roble et al.*, 1988; *Wang*, 1998]. The time integration is explicit in the horizontal direction and implicit in the vertical direction.

The lower boundary condition is specified by assuming chemical equilibrium between ion species. The top boundary condition is given in terms of the ambipolar diffusive flux of O^+:

$$-b_z^2 D_A (2T_p \frac{\partial}{\partial z} + \frac{m_i g}{R^*}) n_i = \Phi_i \tag{6}$$

where D_A is the ambipolar diffusion coefficient, $T_p = (T_i + T_e)/2$ is plasma temperature, R^* is the universal gas constant, m_i is the mass of O^+, and b_z is the vertical component of

the magnetic field. Φ_i is the ambipolar diffusion flux of O^+ at the top boundary, describing the O^+ transport to and from the plasmasphere. It is usually upward (positive) during the day and downward at night (negative). In the model it depends on magnetic latitude and solar local time, and its maximum magnitudes for day and night can be specified separately ($\pm 2\times10^8$ cm^{-2}s^{-1} is currently used for day and night, respectively). A detailed description of this dependence can be found in *Wang* [1998].

Further detail concerning the O^+ transport calculation is given in Appendix B. This description is derived from TIE-GCM documentation, and subroutine and variable names, etc., may differ from the WACCM-X implementation.

2.2.3 Metastable O^+ chemistry and energetics

The ion chemistry in WACCM-X 1.0 was modified to include ionization of the excited metastable ion species $O^+(^2D)$ and $O^+(^2P)$ and their loss reactions. These have a small effect on E-region chemistry, but are significant in the F-region because they provide more rapid paths for transfer of ionization to molecules and their subsequent neutralization through dissociative recombination, thus reducing total plasma density. These reactions also contribute to chemical heating through their exothermicity, so including them raises the neutral temperature of the upper thermosphere by about 50 to 100 K. Earlier model versions that did not include the metastable ions put all of the ionization into $O^+(^4S)$, thereby neglecting the additional solar energy that goes into the excited states, and ultimately into the neutral heating rate. Ionization/excitation rates are included in the solar parameterization described in the next section, and chemical reaction rates are adopted from *Roble* [1995].

2.2.4 Solar EUV ionization and heating

The solar extreme-ultraviolet (EUV) variability and energy deposition scheme, including photoelectron effects, is described in *Solomon and Qian* [2005], and is essentially unchanged from earlier versions of WACCM and WACCM-X, except for a correction to the molecular oxygen cross section in the 105-121 nm band as described by *Garcia et al.* [2014]. However, an optional file-based input now provides a means for running the model with any solar spectral input. This includes solar flare simulation capability, with solar spectra input at a five-minute cadence to match the physics/chemistry time step. Solar spectra can be from either high-time-resolution models, or measurements. Solar spectra estimated by the Flare Irradiance Spectral Model (FISM) [*Chamberlin et al.*, 2007, 2008] are used as the default solar flare spectra input in the current version [cf. *Qian et al.*, 2010].

At night, the lower ionosphere does not entirely disappear, due to some EUV photons multiply-scattered by the exosphere reaching the nightside of the Earth. Starlight may also contribute to night time ionization, but this is currently neglected in WACCM-X. A simplified estimation of this background ionization is applied equally to all model columns, including on the dayside. For consistency, the method used in the TIE-GCM, the TIME-GCM, and the Global Airglow model, is adapted [*Solomon*, 2017]. This considers the primary sources of night ionization to be geocoronal emissions by hydrogen (H Lyman-alpha at 121.6 nm and H Lyman-beta at 102.6 nm) and helium (He I at 58.4 nm and He II at 30.4 nm). These are absorbed using a nominal cross section for each line, and distributed through the column using Beer's law, imagining an overhead, invariant flux. This is a gross approximation to the actual geocoronal illumination, but results in reasonable comparison with observations of the nightside ionosphere, with ion density around 10^3 cm^{-3} in the E-region (~100–150 km) and 10^2 cm^{-3} in the D region (~80–100 km). A more sophisticated parameterization, for future consideration, is provided by *Titheridge* [2003].

2.2.5 High-latitude Ionospheric Inputs

At high latitudes, the effects of the magnetospheric current system are applied using an electric potential pattern and an auroral precipitation oval. The *Heelis et al.* [1982] empirical specification of potential, parameterized by the geomagnetic Kp index as described by *Emery et al.* [2012], is employed, and ionization from auroral precipitation is specified using the formulation described by *Roble and Ridley* [1987], based on the estimated hemispheric power of precipitating electrons. The empirical estimate of this power as it depends on Kp has been increased from the original formulation by an approximate factor of two for high Kp, based on results obtained by *Zhang and Paxton* [2008] from the Global Ultraviolet Imager (GUVI) on the TIMED satellite. These results give a hemispheric power of, for example, ~40 GW at Kp=3, increasing to ~150 GW at Kp=7 [*Solomon et al.*, 2012].

2.2.6 Electron and Ion Temperature

A complete treatment of electron temperature would consider the adiabatic expansion, heat advection, electron heat flux due to electric current and thermal conduction, heating associated with production of electron-ion pairs due to photochemical and auroral processes, and cooling due to collisions with neutral and ion species. In the terrestrial ionosphere, however, adiabatic expansion and heat advection are negligible. Furthermore, with the assumptions that the electron heat flux being along the magnetic field lines and the field-aligned currents not present, and the dominant temperature gradients being in the vertical, only thermal conduction in the vertical direction is considered for the ionosphere [e.g. *Rees and Roble*, 1975; *Schunk and Nagy*, 2009]

$$\frac{3}{2} n_e k \frac{\partial T_e}{\partial t} = \sin^2 I \frac{\partial}{\partial z}(\mu_e \frac{\partial T_e}{\partial z}) + \sum Q_e - \sum L_e \tag{7}$$

where n_e, T_e are electron number density and electron temperature, μ_e the electron thermal conductivity, $\sum Q_e$ and $\sum L_e$ are total heating and cooling rates, respectively, and I is the geomagnetic dip angle. Calculation of μ_e follows the formulation given by *Rees and Roble* [1975] (also used in TIE-GCM). The total heating rate is proportional to the production rates of electron-ion pairs from all photochemical reactions (including those involving metastable O^+ states) and auroral processes. The heating efficiency uses the empirical formulation by *Swartz and Nisbet* [1972] and will be updated to the new formulation of *Smithtro and Solomon* [2008]. The cooling rates include electron energy loss through collisions with ions and neutrals, and the formulations follow that of *Rees and Roble* [1975] (again the same as those used in TIE-GCM). The energy loss to the neutrals is then used to calculate the heating of neutrals by thermal electrons.

Equation 7 could be further simplified by making a quasi-steady state assumption, which is the approach taken in the TIE-GCM formulation. However, a numerical study by *Roble and Hastings* [1977] found that between 300-600 km altitude, it would take 200-1000 seconds to reach steady state. With the usual time step of 300 seconds in WACCM-X, the steady state assumption may not be valid. Therefore, a time-dependent equation 7 is solved in WACCM-X, using the Crank-Nicolson method. Because the equation is highly nonlinear, the solver is applied iteratively to obtain convergence.

The following empirical topside heat flux has been used at the upper boundary in the TIE-GCM and is adapted here:

$$F^e_{top} = \begin{cases} F^{eD}_{top} & \text{if } \zeta \le 80^\circ \\ (F^{eD}_{top} + F^{eN}_{top})/2 + (F^{eD}_{top} - F^{eN}_{top})/2 \cos(\frac{\zeta - 80^\circ}{20^\circ}\pi) & \text{if } 80^\circ < \zeta < 100^\circ \\ F^{eN}_{top} & \text{if } \zeta \ge 100^\circ \end{cases} \tag{8}$$

where ζ is solar zenith angle, and the daytime and nighttime heating flux F_{top}^{eD} and F_{top}^{eN} are defined as

$$F_{top}^{eD} = \begin{cases} -2.25 \times 10^7 F10.7(1 + \sin(\frac{|\phi_M|-30^\circ}{60^\circ}\pi))/2 & \text{if } |\phi_M| < 60^\circ \\ -2.25 \times 10^7 F10.7 & \text{if } |\phi_M| \geq 60^\circ \end{cases} \quad (9)$$

$$F_{top}^{eN} = F_{top}^{eD}/5 \quad (10)$$

where ϕ_M is the geomagnetic latitude, and F10.7 is the solar 10.7 cm radio flux with solar flux unit (sfu, 1 sfu = $10^{-22} Wm^{-2} Hz^{-1}$). The unit of the heat flux is $eVcm^{-2}s^{-1}$

The ion temperature T_i is calculated by assuming equilibrium between the heating of the ions by electron-ion Coulomb interactions, Joule heating and the cooling through ion-neutral collisions [e.g. *Schunk and Nagy*, 2009].

2.3 Model structure and configuration

The ionospheric wind dynamo and O^+ transport in the F-region are solved using geomagnetic coordinates and geographic coordinates, respectively, as discussed in previous sections. WACCM-X ionosphere modules are coupled to the physics decomposition via an interface layer (ionosphere_interface). The ionosphere interface layer implemented uses the FV dynamics-physics (DP) coupling methodology, which has access to physical quantities in geographic coordinates, and also provides the infrastructure to distribute the output of the ionospheric modules, along with updates from dynamical core calculations, to the column physics decomposition. Figure 1 is a schematic diagram showing how the ionosphere_interface module interacts with other model components. As noted above, ESMF parallel mapping routines are used to transform fields between the geographic and geomagnetic grids. Other ionosphere models will need to provide an ionosphere_interface module that could be modeled after WACCM-X's interface module.

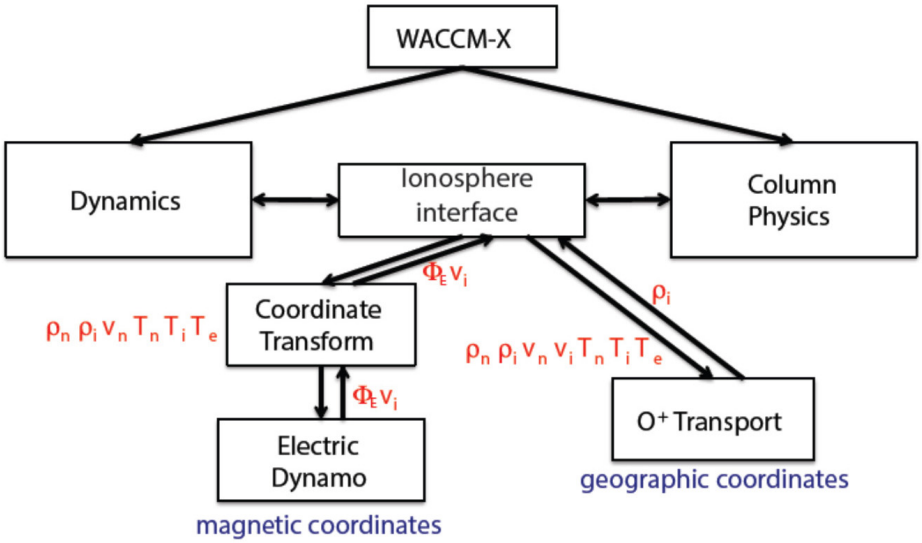

Figure 1. Schematic diagram describing the coupling of the ionospheric modules with other model components through the ionosphere_interface module. ρ, $\mathbf{v}$ and T are density, velocity, and temperature, respectively, with subscripts n, i and e denoting neutral, ion and electron, respectively. Φ_E is the electric potential.

A five-minute time step is used for advancing tendencies in column physics, while sub-cycling is used for dynamics and species transport due to large wind velocities, especially in the thermosphere (the default sub-cycling is 8 dynamical time steps per every physics time step). The time-step and the sub-cycling number can be adjusted as needed. By comparison, CAM and regular WACCM generally use a 30-minute physics time step. Since WACCM-X has more altitude levels and performs additional ionospheric calcula-

tions, it is therefore a relatively computationally intensive model. However, it scales reasonably well in the current parallel implementation, for example, one model year runs in 0.75 days of wall-clock time on 864 cores (24 nodes on the NCAR supercomputer "cheyenne"), which is a model-time to real-time ratio of almost 500.

3 Summary and Future Plans

The current version of WACCM-X is capable of reproducing the climatological ionosphere-thermosphere state, as well as variability on hourly to daily time scales due to both geomagnetic and lower atmosphere forcing. Despite the general agreement of our current model with the climalogical ionosphere and thermosphere features, we envisage several areas of further improvements. More specifically, areas of active model development which we believe will considerably enhance the scientific value of WACCM-X simulation results are briefly detailed in the following.

WACCM-X is currently limited in its ability to simulate geomagnetic activity due to the use of the Heelis convection pattern at high-latitudes. There exist alternative methods for specifying the high-latitude electric potential and auroral precipitation. These include the *Weimer* [2005] empirical model driven by observed upstream IMF conditions, as well as data assimilative schemes such as the Assimilative Mapping of Ionosphere Electrodynamics (AMIE) procedure [*Richmond and Kamide*, 1988]. Implementation of these alternative methods for high-latitude forcing specification will lead to improved simulations of storm time ionosphere-thermosphere variability.

Pedatella et al. [2014] implemented the data assimilation capability into WACCM using the Data Assimilation Research Testbed (DART) ensemble Kalman filter. This work is currently being extended to WACCM-X so that the model meteorology can be constrained by the assimilation of lower and middle atmosphere observations. This will enhance the capability of the model to reproduce ionosphere-thermosphere variability driven by the lower atmosphere. In the future, data assimilation will be extended into the upper atmosphere through assimilation of ground and satellite observations, such as from the upcoming COSMIC-2, GOLD, and ICON satellite missions. This will further constrain the model state, leading to a whole atmosphere-ionosphere reanalysis.

WACCM-X is built upon the chemistry, dynamics, and physics of CAM4 and WACCM4. Both CAM and WACCM have seen their own significant recent developments, including increased horizontal resolution, and CAM6 and WACCM6 will be released as part of CESM 2.0. The latest versions of CAM and WACCM additionally include updated convection and gravity wave drag parameterization schemes. These can indirectly impact the upper atmosphere through improved representation of middle atmosphere circulation, as well as better simulation of tidal forcing and variability due to latent heating. Future versions of WACCM-X will incorporate the recent improvements in the lower and middle atmosphere components of CESM, and will have increased horizontal resolution.

WACCM-X 2.0 is released as an optional configuration of CESM 2.0. It currently is installed on the NCAR supercomputers and is available to any researcher with access to those machines. It is an open-source community model, which can be installed on any computer of sufficient capability that supports the necessary compilers and libraries. Porting the model to other environments can be accomplished by accessing the information at the NCAR CESM web site and related support pages.

A: Appendix A: Electrodynamics

The basic equations of the steady state electrodynamo are shown in this chapter. If an equation is taken from *Richmond* [1995]. then the additional equation number refers to the equation number in *Richmond* [1995]. In the following the presentation of the equations is based on the coding in the source code and might not look straight forward in many places. For the location in the source code of the equations it is referred to the subroutine names.

For longer time scales it is valid to assume steady state electrodynamics with a divergence free current density $\mathbf{J}$. It is also assumed that the conductivity along the magnetic field line is very high, thus there is no electric field component in this direction. Therefore the electrodynamo equation can be reduced to a two dimensional equation.

The current density is divergence free

$$\nabla \cdot \mathbf{J} = 0 \tag{A.1}$$

The current density has an ohmic component transverse to the magnetic field and parallel to the magnetic field line $\mathbf{J}_{||}$ and a non–ohmic magnetospheric component $\mathbf{J}_M$. The total current density is expressed by (eq. 2.1 in *Richmond* [1995])

$$\mathbf{J} = \sigma_P(\mathbf{E} + \mathbf{u} \times \mathbf{B}) + \sigma_H \mathbf{b} \times (\mathbf{E} + \mathbf{u} \times \mathbf{B}) + \mathbf{J}_{||} + \mathbf{J}_M \tag{A.2}$$

with σ_P and σ_H the Pedersen and Hall conductivities. The neutral wind is denoted by $\mathbf{u}$, the electric field by $\mathbf{E}$ and the geomagnetic field by $\mathbf{B}$ with $\mathbf{b}$ the unit vector parallel to $\mathbf{B}$.

The following relations are used to derive the electrodynamo equation. For details it is referred to *Richmond* [1995]. Apex coordinates are used with two sets of base vectors $\mathbf{e}_i$ and $\mathbf{d}_j$ which are calculated in subroutine apxparm. The directions of $\mathbf{e}_1$ and $\mathbf{d}_1$ are more or less in magnetic eastward, $\mathbf{e}_2$ and $\mathbf{d}_2$ in downward or equatorward, and $\mathbf{e}_3$ and $\mathbf{d}_3$ in field line direction. (eq. 3.11- 3.13 in *Richmond* [1995])

$$\mathbf{e}_1 = \mathbf{d}_2 \times \mathbf{d}_3 \tag{A.3}$$
$$\mathbf{e}_2 = \mathbf{d}_3 \times \mathbf{d}_1 \tag{A.4}$$
$$\mathbf{e}_3 = \mathbf{d}_1 \times \mathbf{d}_2 \tag{A.5}$$

with (eq. 3.8- 3.10 in *Richmond* [1995])

$$\mathbf{d}_1 = R_0 cos\lambda_m \nabla \phi_m \tag{A.6}$$
$$\mathbf{d}_2 = -R_0 sin I_m \nabla \lambda_m \tag{A.7}$$
$$\mathbf{d}_3 = \frac{\mathbf{b_0}}{|\mathbf{d}_1 \times \mathbf{d}_2|} \tag{A.8}$$

The geomagnetic longitude and apex latitude are ϕ_m and λ_m, I_m is the inclination of the geomagnetic field, R_0 the radius to the reference height $R_E + h_0$, and b_0 the unit vector in the direction of the geomagnetic field. The neutral wind $\mathbf{u}$ and the electric field $\mathbf{E}$ can be expressed in terms of the base vectors which has the advantage that the components are constant along a magnetic field line (eq. 4.5 in *Richmond* [1995]).

$$\mathbf{u} = u_{e1}\mathbf{e}_1 + u_{e2}\mathbf{e}_2 \quad \text{with} \quad u_{ei} = \mathbf{u} \cdot \mathbf{d}_i \tag{A.9}$$
$$\mathbf{E} = E_{d1}\mathbf{d}_1 + E_{d2}\mathbf{d}_2 \quad \text{with} \quad E_{di} = \mathbf{E} \cdot \mathbf{e}_i \tag{A.10}$$

The geomagnetic field $\mathbf{B}$ is approximated by the main field $\mathbf{B}_0$. We employ the International Geomagnetic Reference Field (IGRF), including secular variation, and ignore the magnetic perturbation $\Delta\mathbf{B}$ due to external currents (eq. 3.10, 3.15, 4.4 in *Richmond* [1995]).

$$\mathbf{B}_0 = \mathbf{B}_{e3}\mathbf{e}_3 \tag{A.11}$$
$$\mathbf{b}_0 = \mathbf{d}_3 D \quad \text{with} \quad D = |\mathbf{d}_1 \times \mathbf{d}_2| \tag{A.12}$$

The current density can be expressed by

$$\mathbf{J} = \sum_{i=1}^{3} J_{ei}\mathbf{e}_i \text{ with } J_{ei} = \mathbf{J}\cdot\mathbf{d}_i \tag{A.13}$$

Using all the equations from above leads to the current density components J_{e1} and J_{e2} (eq. 5.7, 5.8 in *Richmond* [1995])

$$J_{e1} = \sigma_P d_1^2(E_{d1} + u_{e2}B_{e3}) + (\sigma_H \mathbf{d}_1\cdot\mathbf{d}_2 - \sigma_H D)(E_{d2} - u_{e1}B_{e3}) \tag{A.14}$$

$$J_{e2} = (\sigma_P \mathbf{d}_1\cdot\mathbf{d}_2 + \sigma_H D)(E_{d1} + u_{e2}B_{e3}) + \sigma_P d_2^2(E_{d2} - u_{e1}B_{e3}) \tag{A.15}$$

The height integrated current density in magnetic eastward and downward/ equatorward direction are $K_{m\phi}$ and $K_{m\lambda}$. Knowing the current density $\mathbf{J}$ the height integrated components can be calculated by (eq. 5.1, 5.2 in *Richmond* [1995])

$$K_{m\phi} = |sinI_m| \int_{s_L}^{s_U} \frac{J_{e1}}{D} ds \tag{A.16}$$

$$K_{m\lambda} = \mp \int_{s_L}^{s_U} \frac{J_{e2}}{D} ds \tag{A.17}$$

with the index $(\cdot)_m$ standing for modified apex. The integration is done along the field line and s_L and s_U are the lower and upper boundary of the ionosphere, i.e., approximately 90 km to the top of the model. The electrostatic field is the gradient of the electric potential. Therefore the component of the electric field are (eq. 5.9, 5.10 in *Richmond* [1995])

$$E_{m\phi} = E_{d1} = -\frac{1}{Rcos\lambda_m}\frac{\partial\Phi}{\partial\phi_m} \tag{A.18}$$

$$E_{m\lambda} = -E_{d2}sinI_m = -\frac{1}{R}\frac{\partial\Phi}{\partial\lambda_m} \tag{A.19}$$

Inserting equations (A.18) and (A.19) into the current density component expressions (A.14) and (A.15), which then can be used to calculate the height integrated current density in equations (A.16) and (A.17). This leads to (eq. 5.11, 5.12 in *Richmond* [1995])

$$K_{m\phi} = \Sigma_{\phi\phi}E_{m\phi} + \Sigma_{\phi\lambda}E_{m\lambda} + K^D_{m\phi} \tag{A.20}$$

$$K_{m\lambda} = \Sigma_{\lambda\phi}E_{m\phi} + \Sigma_{\lambda\lambda}E_{m\lambda} + K^D_{m\lambda} \tag{A.21}$$

The terms $K^D_{m\phi}$ and $K^D_{m\lambda}$ are the wind driven height integrated current densities which are the driving forces (eq. 5.19, 5.20 in *Richmond* [1995]).

$$K^D_{m\phi} = B_{e3}|sinI_m| \int_{s_L}^{s_U} \Big[\frac{\sigma_P d_1^2}{D}u_{e2} + \big(\sigma_H - \frac{\sigma_P \mathbf{d}_1\cdot\mathbf{d}_2}{D}\big)u_{e1}\Big] ds \tag{A.22}$$

$$K^D_{m\lambda} = \mp B_{e3} \int_{s_L}^{s_U} \Big[\big(\sigma_H + \frac{\sigma_P \mathbf{d}_1\cdot\mathbf{d}_2}{D}\big)u_{e2} - \frac{\sigma_P d_2^2}{D}u_{e1}\Big] ds \tag{A.23}$$

The conductances in the equations (A.20) and (A.21) are (eq. 5.13–5.18 in *Richmond* [1995])

$$\Sigma_{\phi\phi} = |sinI_m| \int_{s_L}^{s_U} \frac{\sigma_P d_1^2}{D} ds \tag{A.24}$$

$$\Sigma_{\lambda\lambda} = \frac{1}{|sinI_m|} \int_{s_L}^{s_U} \frac{\sigma_P d_2^2}{D} ds \tag{A.25}$$

$$\Sigma_H = \int_{s_L}^{s_U} \sigma_H ds \tag{A.26}$$

$$\Sigma_C = \int_{s_L}^{s_U} \frac{\sigma_P \mathbf{d}_1\cdot\mathbf{d}_2}{D} ds \tag{A.27}$$

$$\Sigma_{\phi\lambda} = \pm(\Sigma_H - \Sigma_C) \tag{A.28}$$

$$\Sigma_{\lambda\phi} = \mp(\Sigma_H + \Sigma_C) \tag{A.29}$$

$$\tag{A.30}$$

Since current continuity applies, the divergence of the horizontal current $K_{m\phi}$ and $K_{m\lambda}$ has to be balanced by an upward current density J_{mr} at the top of the ionospheric current sheet layer. (eq. 5.3 in *Richmond* [1995])

$$J_{mr} = \frac{-1}{Rcos\lambda_m}\left(\frac{\partial K_{m\phi}}{\partial \phi_m} + \frac{\partial K_{m\lambda} cos\lambda_m}{\partial \lambda_m}\right) \tag{A.31}$$

Inserting the height integrated current densities (A.20) and (A.21) into equation (A.31) and assuming that in the closed field line region the field lines are equipotential leads to (eq. 5.23 in *Richmond* [1995])

$$\begin{aligned} &\frac{\partial}{\partial \phi_m}\left(\frac{\Sigma^T_{\phi\phi}}{cos\lambda_m}\frac{\partial \Phi}{\partial \phi_m} + \Sigma^T_{\phi\lambda}\frac{\partial \Phi}{\partial |\lambda_m|}\right) + \frac{\partial}{\partial |\lambda_m|}\left(\Sigma^T_{\lambda\phi}\frac{\partial \Phi}{\partial \phi_m} + \Sigma^T_{\lambda\lambda} cos\lambda_m \frac{\partial \Phi}{\partial |\lambda_m|}\right) \\ &= R\frac{\partial K^{DT}_{m\phi}}{\partial \phi_m} + R\frac{\partial K^{DT}_{m\lambda cos\lambda_m}}{\partial |\lambda_m|} + R^2 cos\lambda_m J_{Mr} \end{aligned} \tag{A.32}$$

with $\frac{\partial}{\partial |\lambda_m|} = -\frac{\partial^{SH}}{\partial \lambda_m} = \frac{\partial^{NH}}{\partial \lambda_m}$ and $J_{Mr} = J^{SH}_{mr} + J^{NH}_{mr}$. The values $(\cdot)^T$ denote the sum of the values from northern $(\cdot)^{NH}$ and southern $(\cdot)^{SH}$ hemisphere (eq. 5.24–5.29 *Richmond* [1995])

$$\Sigma^T_{\phi\phi} = \Sigma^{NH}_{\phi\phi} + \Sigma^{SH}_{\phi\phi} \tag{A.33}$$

$$\Sigma^T_{\lambda\lambda} = \Sigma^{NH}_{\lambda\lambda} + \Sigma^{SH}_{\lambda\lambda} \tag{A.34}$$

$$\Sigma^T_{\lambda\phi} = \Sigma^{NH}_{\lambda\phi} - \Sigma^{SH}_{\lambda\phi} \tag{A.35}$$

$$\Sigma^T_{\phi\lambda} = \Sigma^{NH}_{\phi\lambda} - \Sigma^{SH}_{\phi\lambda} \tag{A.36}$$

$$K^{DT}_{m\phi} = K^{D,NH}_{m\phi} + K^{D,SH}_{m\phi} \tag{A.37}$$

$$K^{DT}_{m\lambda} = K^{D,NH}_{m\lambda} - K^{D,SH}_{m\lambda} \tag{A.38}$$

In the source code the electrodynamo equation (A.32) is divided by $\frac{\partial \lambda_m}{cos\lambda_0 \partial \lambda_0}$ with λ_0 the equally spaced distribution in modified apex latitudes λ_m which is irregularly spaced.

B: Appendix B: O^+ Transport

Most ion species are in photochemical equilibrium below 1000 km, and can be simply calculated by balancing the production and loss rates. However, O^+ is determined by considering diffusion, along the magnetic field line and the $\mathbf{E} \times \mathbf{B}$ transport. In the following for simplicity the variable n is used for the O^+ number density $n(O^+)$.

$$\frac{\partial n}{\partial t} - Q + Ln = -\nabla \cdot (n\mathbf{v}_i) \tag{B.1}$$

with n the O^+ number density, Q the production rate of O^+, L the loss rate of O^+. The right hand side is the transport due $\mathbf{E} \times \mathbf{B}$ drift and the field aligned ambipolar diffusion. The ion velocity $\mathbf{v}_i$ is given by

$$\mathbf{v}_i = \mathbf{v}_{i,\parallel} + \mathbf{v}_{i,\perp} \tag{B.2}$$

with the parallel and perpendicular velocity with respect to the geomagnetic field

$$\mathbf{v}_{i,\parallel} = \left[\mathbf{b} \cdot \frac{1}{\nu_{in}} \left(\mathbf{g} - \frac{1}{\rho_i}\nabla(P_i + P_e)\right) + \mathbf{b} \cdot \mathbf{v}_n\right]\mathbf{b} \tag{B.3}$$

$$\mathbf{v}_{i,\perp} = \frac{\mathbf{E} \times \mathbf{B}}{|B|} \tag{B.4}$$

The parallel velocity is caused by ambipolar diffusion and the perpendicular velocity by $\mathbf{E} \times \mathbf{B}$ drift velocity. The unit vector along the geomagnetic field line is $\mathbf{b}$, ν_{in} is the O^+ ion-neutral collision frequency, $\mathbf{g}$ the gravitational acceleration due to gravity, ρ_i is the ion mass density, P_i and P_e are the ion and electron pressure, $\mathbf{v}_n$ is the neutral velocity, $|B|$ is the geomagnetic field strength, and $\mathbf{E}$ is the electric field.

Inserting the parallel (B.3) and perpendicular (B.4) velocity into the O^+ transport equation (B.1) leads to

$$\begin{aligned}
&\frac{\partial n}{\partial t} - Q + Ln + [(\mathbf{b}_h \cdot \nabla_h)Kb_z]\left[\left(\frac{1}{H}\frac{\partial}{\partial Z}(2T_p n) + \frac{mg}{k_B}n\right)\right] \\
&- (\mathbf{b}_h \cdot \nabla_h)(\mathbf{b} \cdot v_n n) + \left(b_z \frac{1}{H}\frac{\partial}{\partial Z} + \nabla \cdot \mathbf{b}\right) Kb_z \left(\frac{1}{H}\frac{\partial}{\partial Z}(2T_p n) + \frac{mg}{k_B}n\right) - \\
&\left(b_z \frac{1}{H}\frac{\partial}{\partial Z} + \nabla \cdot \mathbf{b}\right)(\mathbf{b} \cdot v_n n) - \left[B^2 \mathbf{v}_{ExB,h} \cdot \nabla\left(\frac{n}{B^2}\right)\right]_H - \\
&B^2 \mathbf{v}_{ExB,z} \frac{1}{H}\frac{\partial}{\partial Z}\left(\frac{n}{B^2}\right) + (\mathbf{b}_H \cdot \nabla_H) K (\mathbf{b}_H \cdot \nabla_H)(2nT_p) + \\
&Kb_z (\mathbf{b}_H \cdot \nabla_H)\left(\frac{1}{H}\frac{\partial}{\partial Z}(2T_p n) + \frac{mg}{k_B}n\right) + \\
&\left(b_z \frac{1}{H}\frac{\partial}{\partial Z} + \nabla \cdot \mathbf{b}\right) K \left(\mathbf{b}_H \cdot \nabla_H (2nT_p)\right) = 0
\end{aligned} \tag{B.5}$$

where the ambipolar diffusion coefficient is $K = D_A + K_E$ with K_E the eddy diffusion coefficient in the lower thermosphere, and D_A the molecular diffusion coefficient. The geomagnetic unit vector, the horizontal vector and vertical component are $\mathbf{b}$, $\mathbf{b}_H$ and b_z respectively. The scale height is denoted by H, $\mathbf{v}_{ExB,h}$ is the horizontal drift vector, and $\mathbf{v}_{ExB,z}$ the vertical component. The horizontal derivative of ∇ is ∇_H. The plasma pressure is $T_p = \frac{1}{2}(T_e + T_i)$.

The fourth, eleventh, and sixth term are the contributions of the vertical component of ambipolar diffusion to the plasma transport due to respectively, the horizontal variation of the diffusion coefficient and b_z, the horizontal variation of the vertical ambipolar diffusion, and the vertical variation of the vertical ambipolar diffusion. The tenth term is the contribution of the horizontal component of the ambipolar diffusion due to variations in the vertical and horizontal direction. The fifth and seventh term are the neutral wind effects on the O^+ distribution, and the eight and ninth terms are the effects of the $\mathbf{E} \times \mathbf{B}$ transport.

The flux at the upper boundary is determined in the subroutine oplus_flux. The transport from and to the plasmasphere is specified by the flux Φ. The latitudinal variation of the flux is specified by the factor A

$$\begin{aligned} A =& 1 && \text{for} |\lambda_m| \geq \frac{\Pi}{24} \\ A =& \frac{1}{2}\left(1 + \sin \Pi \frac{|\lambda_m| - \frac{\Pi}{48}}{\Pi/24}\right) && \text{for} |\lambda_m| < \frac{\Pi}{24} \end{aligned} \tag{B.6}$$

with $A \geq 0.05$, and λ_m the geomagnetic latitude. The daytime flux is Φ_D^o and upward, and the nighttime flux Φ_N^o which is downward

$$\begin{aligned} \Phi_D^o &= 2 \cdot 10^8 \\ \Phi_N^o &= -2 \cdot 10^8 \end{aligned} \tag{B.7}$$

and the flux variation during the day– and nighttime is given by

$$\begin{aligned} F_{eD} =& \Phi_D^o A \\ F_{eN} =& \Phi_N^o A \end{aligned} \tag{B.8}$$

The solar zenith angle ψ determines which flux F^{O^+} is used

$$\begin{aligned} F^{O^+} &= F_{eN} \quad \text{for} \quad \psi \geq 80^o \\ F^{O^+} &= F_{eD} \quad \text{for} \quad \psi < 100^o \end{aligned} \tag{B.9}$$

with

$$F^{O^+} = \frac{1}{2}[F_{eD} + F_{eN}] + \frac{1}{2}[F_{eD} - F_{eN}] \cos(\Pi \frac{\psi - 80}{20}) \quad \text{for} \quad 80^o < \psi < 100^o \tag{B.10}$$

The divergence of the geomagnetic field vector $\mathbf{b}$ is determined in subroutine divb. Since variation in height of the geomagnetic field is neglected the divergence also varies only with latitude and longitude.

$$\begin{aligned} \nabla \cdot \mathbf{b} =& \frac{b_x(\phi + \Delta\phi, \lambda) - b_x(\phi - \Delta\phi, \lambda)}{2\Delta\phi R_E \cos\lambda} + \\ & \frac{\cos\lambda + \Delta\lambda b_y(\phi, \lambda + \Delta\lambda) - \cos\lambda - \Delta\lambda b_y(\phi, \lambda - \Delta\lambda)}{2\Delta\lambda R_E \cos\lambda} + \\ & \frac{2b_z(\phi, \lambda)}{R_E} \end{aligned} \tag{B.11}$$

with b_y the northward, b_x the eastward, and b_z the upward component of the unit geomagnetic field vector $\frac{\mathbf{B}}{|B|}$. The divergence is stored in the value dvb.

In the first latitudinal scan the plasma pressure is determined at $\lambda - \Delta\lambda$, λ and , $\lambda + \Delta\lambda$, e.g. at λ

$$T_p(\phi, \lambda, z + \frac{1}{2}\Delta z) = \frac{1}{2}(T_i + T_e) \tag{B.12}$$

The values in the code are stored in the variable tpj.

In subroutine rrk the diffusion coefficient are determined. The values are stored in the variable dj in the source code at $\lambda - \Delta\lambda$, λ and , $\lambda + \Delta\lambda$.

$$D_A = \frac{1.42 \cdot 10^{17} k_B T_n}{p\overline{m}\left[\frac{\Psi_O}{m_O}\sqrt{T_p}(1 - 0.064 log_{10} T_p)^2 C_f + 18.6\frac{\Psi_{N_2}}{m_{N_2}} + 18.1\frac{\Psi_{O_2}}{m_{O_2}}\right]} \tag{B.13}$$

with the pressure $p(z + \frac{1}{2}\Delta) = p_0 e^{-z - \frac{1}{2}\Delta z}$, the number density of N_2 is $\Psi_{N_2} = 1 - \Psi_{O_2} - \Psi_O$, the factor is $C_f = 1.5$, and $N = \frac{p_0 e^{-z - \frac{1}{2}\Delta z}}{k_B T_n}$. The value D_A is determined at half pressure

levels e.g. $z + \frac{1}{2}\Delta z$. The variable tpj holds $2T_p$ at the midpoint pressure level $z + \frac{1}{2}\Delta z$ and at the latitudes $\lambda - \Delta\lambda$, λ and , $\lambda + \Delta\lambda$. The scale height is also determined at the midpoint pressure level, and the latitudes $\lambda - \Delta\lambda$, λ and , $\lambda + \Delta\lambda$.

$$H = \frac{R^* T_n}{\overline{m} g} \tag{B.14}$$

The scale height is stored in the variable hj. The dot product $\mathbf{b} \cdot \mathbf{v}_n n$ is stored in bvel and calculated also on the midpoint pressure level, and the latitudes $\lambda - \Delta\lambda$, λ and , $\lambda + \Delta\lambda$.

$$\mathbf{b} \cdot \mathbf{v}_n n = \left[b_x u_n + b_y v_n + b_z \frac{W(z) + W(z + \frac{1}{2}\Delta z)}{2} H(z + \frac{1}{2}\Delta z) \right] n \tag{B.15}$$

In subroutine diffus the term $\left[2\frac{\partial T_p n}{H \partial Z} + \frac{m_{O^+} g}{R^*} n \right]$ at the midpoint pressure level is determined

$$\begin{aligned} F(z + \frac{1}{2}\Delta z) = & \frac{1}{2H(z + \frac{1}{2}\Delta z)\Delta z} [2T_p(z + \frac{3}{2}\Delta z) n(z + \frac{3}{2}\Delta z) - \\ & 2T_p(z - \frac{1}{2}\Delta z) n(z - \frac{1}{2}\Delta z)] + \frac{m_{O^+} g}{R^*} n(z + \frac{1}{2}\Delta z) \end{aligned} \tag{B.16}$$

The term is stored in the variable diffj. The upper and lower boundary values are set by

$$\begin{aligned} F(z_{bot} + \frac{1}{2}\Delta z) = & \frac{1}{H(z_{bot} + \frac{1}{2}\Delta z)\Delta z} [2T_p(z_{bot} + \frac{3}{2}\Delta z) n(z_{bot} + \frac{3}{2}\Delta z) - \\ & 2T_p(z_{bot} + \frac{1}{2}\Delta z) n(z_{bot} + \frac{1}{2}\Delta z)] + \frac{m_{O^+} g}{R^*} n(z_{bot} + \frac{1}{2}\Delta z) \end{aligned} \tag{B.17}$$

$$\begin{aligned} F(z_{top} - \frac{1}{2}\Delta z) = & \frac{1}{H(z_{top} - \frac{1}{2}\Delta z)\Delta z} [2T_p(z_{top} - \frac{1}{2}\Delta z) n(z_{top} - \frac{1}{2}\Delta z) - \\ & 2T_p(z_{top} - \frac{3}{2}\Delta z) n(z_{top} - \frac{3}{2}\Delta z)] + \frac{m_{O^+} g}{R^*} n(z_{top} - \frac{1}{2}\Delta z) \end{aligned} \tag{B.18}$$

The value $2nT_p$ is determined at midpoint level, and the latitudes $\lambda - \Delta\lambda$, λ and , $\lambda + \Delta\lambda$. The value overwrites the variable tpj. The latitudinal smoothed value of $n(O^+)^{t_n - \Delta t}$ are determined by

$$\begin{aligned} n(O^+)^{smo\lambda, t_n - \Delta t} = & n(O^+)^{t_n - \Delta t} - f_{smo} [n(O^+)^{t_n - \Delta t}(\lambda + 2\Delta\lambda) + \\ & n(O^+)^{t_n - \Delta t}(\lambda - 2\Delta\lambda) - 4(n(O^+)^{t_n - \Delta t}(\lambda + \Delta\lambda) + \\ & n(O^+)^{t_n - \Delta t}(\lambda - \Delta\lambda)) + 6n(O^+)^{t_n - \Delta t}(\lambda)] \end{aligned} \tag{B.19}$$

and stored in optm1_smooth, and $f_{smo} = 0.003$.

The second latitudinal scan starts with calculating the value of $\mathbf{b} \cdot \nabla_H$ in subroutine bdotdh at the midpoint level. The output variable is bdotdh_op. The input is the term from eq. (B.16) $F = \left[2\frac{\partial T_p n}{H \partial Z} + \frac{m_{O^+} g}{R^*} n \right]$, which leads to $(\mathbf{b} \cdot \nabla_H) \left[2\frac{\partial T_p n}{H \partial Z} + \frac{m_{O^+} g n}{R^*} \right]$

$$\begin{aligned} T1 = & \frac{1}{R_E} [\frac{b_x}{2\Delta\phi \cos\lambda} \{F(\phi + \Delta\phi, \lambda) - F(\phi - \Delta\phi, \lambda)\} + \\ & b_y \frac{F(\phi, \lambda + \Delta\lambda) - F(\phi, \lambda - \Delta\lambda)}{2\Delta\lambda}] \end{aligned} \tag{B.20}$$

The term is multiplied by the diffusion coefficient D_A from subroutine rrk, which leads to

$$D_A(z + \frac{1}{2}\Delta z) b_z (\mathbf{b} \cdot \nabla_H) \left[2\frac{\partial T_p n}{H \partial Z} + \frac{m_{O^+} g}{R^*} n \right] \tag{B.21}$$

The same subroutine bdotdh is used to calculate $\mathbf{b} \cdot \nabla_H \left[2T_p n \right]$. Using eq. (B.20) with $F = 2T_p n$. The values are determined at the midpoint pressure level, and at the latitudes $\lambda - \Delta\lambda$, λ and , $\lambda + \Delta\lambda$. Afterwards the value is multiplied by

$$D_A(z + \frac{1}{2}\Delta z) \mathbf{b} \cdot \nabla_H \left[2T_p n \right] \tag{B.22}$$

and stored in the variable bdotdh_opj.

The third latitudinal scan starts with calling the subroutine bdotdh for the term in eq. (B.22) $F = D_A \mathbf{b} \cdot \nabla_H \left[2T_p n\right]$, which leads to (see eq. (B.20))

$$\mathbf{b} \cdot \nabla_H \left(D_A \mathbf{b} \cdot \nabla_H \left[2T_p n\right]\right) \tag{B.23}$$

evaluated at the midpoint pressure level, and stored in the variable bdotdh_diff.

The subroutine bdzdvb calculates the term $\left(b_z \frac{1}{H} \frac{\partial}{\partial Z} + \nabla \cdot \mathbf{b}\right) G$, with the input into the subroutine $\nabla \cdot \mathbf{B}$, and $G = D_A \mathbf{b} \cdot \nabla_H \left[2T_p n\right]$.

$$\begin{aligned} T3(z + \frac{1}{2}\Delta z)) = & \frac{b_z}{2H(z + \frac{1}{2}\Delta z)\delta z} \left\{ G(z + \frac{3}{2}\Delta z) - G(z - \frac{1}{2}\Delta z) \right\} + \\ & \nabla \cdot \mathbf{b} G(z + \frac{1}{2}\Delta z) \end{aligned} \tag{B.24}$$

At the upper and lower boundary the values are set to

$$\begin{aligned} T3(z_{top} - \frac{1}{2}\Delta z)) = & \frac{b_z}{2H(z_{top} - \frac{1}{2}\Delta z)\delta z} \left\{ G(z_{top} - \frac{1}{2}\Delta z) - G(z_{top} - \frac{3}{2}\Delta z) \right\} + \\ & \nabla \cdot \mathbf{b} G(z_{top} - \frac{1}{2}\Delta z) \end{aligned} \tag{B.25}$$

$$\begin{aligned} T3(z_{bot} + \frac{1}{2}\Delta z)) = & \frac{b_z}{2H(z_{bot} + \frac{1}{2}\Delta z)\delta z} \left\{ G(z_{bot} + \frac{3}{2}\Delta z) - G(z_{bot} + \frac{1}{2}\Delta z) \right\} + \\ & \nabla \cdot \mathbf{b} G(z_{bot} + \frac{1}{2}\Delta z) \end{aligned} \tag{B.26}$$

All the explicit terms are added together from eq. (B.21), (B.22), and (B.24) which leads to

$$\begin{aligned} T_{1,explicit} = & - D_A(z + \frac{1}{2}\Delta z) b_z (\mathbf{b} \cdot \nabla_H) \left[2 \frac{\partial T_p n}{H \partial Z} + \frac{m_{O^+} g}{R^*} n \right] \\ & - \mathbf{b} \cdot \nabla_H \left(D_A \mathbf{b} \cdot \nabla_H \left[2T_p n\right]\right) \\ & - \left(b_z \frac{1}{H} \frac{\partial}{\partial Z} + \nabla \cdot \mathbf{b} \right) \left(D_A \mathbf{b} \cdot \nabla_H \left[2T_p n\right]\right) \end{aligned} \tag{B.27}$$

In addition the term $(\mathbf{b}_H \cdot \nabla_H)(\mathbf{b} \cdot \mathbf{v}_{n,H})$ and $\left[b^2 v_{ExB,H} \cdot \nabla(\frac{n}{B^2})\right]_H$ are treated as explicit terms which leads to

$$\begin{aligned} T_{2,explicit} = & T_{1,explicit} + \frac{1}{2R_E} [\frac{b_x}{\Delta\phi \cos\lambda} \left(\mathbf{b} \cdot \mathbf{v}_n(\phi + \Delta\phi, \lambda) - \mathbf{b} \cdot \mathbf{v}_n(\phi - \Delta\phi, \lambda) \right) + \\ & v_{ExB,x}(z + \frac{1}{2}\Delta z) B^2(\phi, \lambda) \left(\frac{n(\phi + \Delta\phi, \lambda)}{B^2(\phi + \Delta\phi, \lambda)} - \frac{n(\phi - \Delta\phi, \lambda)}{B^2(\phi - \Delta\phi, \lambda)} \right) \\ & + \frac{1}{\Delta\lambda} (b_y \left(\mathbf{b} \cdot \mathbf{v}_n(\phi, \lambda + \Delta\lambda) - \mathbf{b} \cdot \mathbf{v}_n(\phi, \lambda - \Delta\lambda) \right) + \\ & v_{ExB,y}(z + \frac{1}{2}\Delta z) B^2(\phi, \lambda) \left(\frac{n(\phi, \lambda + \Delta\lambda)}{B^2(\phi, \lambda + \Delta\lambda)} - \frac{n(\phi, \lambda - \Delta\lambda)}{B^2(\phi, \lambda - \Delta\lambda)} \right))] \end{aligned} \tag{B.28}$$

Afterwards the following values are set

$$\frac{\nabla \cdot \mathbf{b}}{b_z} \tag{B.29}$$

$$\frac{1}{\Delta z H} \tag{B.30}$$

$$T_p = \frac{1}{2}(T_e + T_i) \tag{B.31}$$

at the midpoint pressure level and stored in the variables dvb, srchdz, and tp respectively.

The term $2T_p \frac{1}{H\Delta z} \pm \frac{gm}{2R^*}$ are determined

$$S_p(z + \frac{3}{2}\Delta z) = 2T_p(z + \frac{3}{2}\Delta z)\frac{1}{H(z + \Delta z)\Delta z} + \frac{gm}{2R^*} \tag{B.32}$$

$$S_m(z + \frac{3}{2}\Delta z) = 2T_p(z + \frac{1}{2}\Delta z)\frac{1}{H(z + \Delta z)\Delta z} - \frac{gm}{2R^*} \tag{B.33}$$

and stored in the variable tphdz1 for S_p and tphdz0 for S_m respectively. The lower boundaries are set by

$$\begin{aligned} S_p(z_{bot} + \frac{1}{2}\Delta z) =& 2T_p(z_{bot} + \frac{1}{2}\Delta z) \\ & \left[\frac{1.5}{H(z_{bot} + \frac{1}{2}\Delta z)\Delta z} - \frac{0.5}{H(z_{bot} + \frac{3}{2}\Delta z)\Delta z}\right] + \frac{gm}{2R^*} \end{aligned} \tag{B.34}$$

$$\begin{aligned} S_m(z_{bot} + \frac{1}{2}\Delta z) =& 2 \cdot \left[2T_p(z_{bot} + \frac{1}{2}\Delta z) - T_p(z_{bot} + \frac{3}{2}\Delta z)\right] \\ & \left[\frac{1.5}{H(z_{bot} + \frac{1}{2}\Delta z)\Delta z} - \frac{0.5}{H(z_{bot} + \frac{3}{2}\Delta z)\Delta z}\right] - \frac{gm}{2R^*} \end{aligned} \tag{B.35}$$

and stored in tphdz1(lev0) and tphdz0(lev0), respectively, with $lev0$ corresponding to $z_{bot} + \frac{1}{2}\Delta z$ on the midpoint pressure level. The upper boundary values are

$$\begin{aligned} S_p(z_{top} + \frac{1}{2}\Delta z) =& 2 \cdot \left[2T_p(z_{top} - \frac{1}{2}\Delta z) - T_p(z_{top} - \frac{3}{2}\Delta z)\right] \\ & \left[\frac{1.5}{H(z_{top} - \frac{1}{2}\Delta z)\Delta z} - \frac{0.5}{H(z_{top} - \frac{3}{2}\Delta z)\Delta z}\right] + \frac{gm}{2R^*} \end{aligned} \tag{B.36}$$

$$\begin{aligned} S_m(z_{top} + \frac{1}{2}\Delta z) =& 2T_p(z_{top} - \frac{1}{2}\Delta z) \\ & \left[\frac{1.5}{H(z_{top} - \frac{1}{2}\Delta z)\Delta z} - \frac{0.5}{H(z_{top} - \frac{3}{2}\Delta z)\Delta z}\right] - \frac{gm}{2R^*} \end{aligned} \tag{B.37}$$

and stored in tphdz1(lev1) and tphdz0(lev1), respectively, with the index $lev1 = nlev + 1$ corresponding to $z_{top} + \frac{1}{2}\Delta z$.

The diffusion coefficient D_A are calculated at the interface pressure level $z, z + \Delta z, ...$ by averaging

$$D_A(z) = \frac{1}{2}\left(D_A(z + \frac{1}{2}\Delta z) + D_A(z - \frac{1}{2}\Delta z)\right) \tag{B.38}$$

and stored in the variable djint. The upper and lower boundary values are determined by extrapolation

$$D_A(z_{bot}) = \frac{1}{2}\left(3D_A(z_{bot} + \frac{1}{2}\Delta z) - D_A(z_{bot} + \frac{3}{2}\Delta z)\right) \tag{B.39}$$

$$D_A(z_{top}) = \frac{1}{2}\left(3D_A(z_{top} - \frac{1}{2}\Delta z) - D_A(z_{top} - \frac{3}{2}\Delta z)\right) \tag{B.40}$$

The term $T_4 = \frac{\nabla\cdot\mathbf{b}}{b_z} + \frac{\mathbf{b}_H\cdot\nabla_H(D_A b_z)}{R_E D_A b_z^2}$ is determined at the midpoint pressure level, and stored in the variable divbz

$$\begin{aligned} T_4(z+\frac{1}{2}\Delta z) = &\frac{\nabla\cdot\mathbf{b}}{b_z}(\phi,\lambda) + \frac{1}{R_E D_A(\phi,\lambda,z+\frac{1}{2}\Delta z)b_z^2}[\\ &\frac{b_x(\phi,\lambda)}{\cos\lambda}(\frac{D_A(\phi+\Delta\phi,\lambda,z+\frac{1}{2}\Delta z)b_z(\phi+\Delta\phi,\lambda)}{2\Delta\phi} - \\ &\frac{D_A(\phi-\Delta\phi,\lambda,z+\frac{1}{2}\Delta z)b_z(\phi-\Delta\phi,\lambda)}{2\Delta\phi})+ \\ &b_y(\phi,\lambda)(\frac{D_A(\phi,\lambda+\Delta\lambda,z+\frac{1}{2}\Delta z)b_z(\phi,\lambda+\Delta\lambda)}{2\Delta\lambda} - \\ &\frac{D_A(\phi,\lambda-\Delta\lambda,z+\frac{1}{2}\Delta z)b_z(\phi,\lambda-\Delta\lambda)}{2\Delta\lambda})] \end{aligned} \tag{B.41}$$

The periodic points for T_4 are set to zero.

The term $T_5 = b_z^2(\frac{1}{H\Delta z} \pm \frac{1}{2}T_4)$ are calculated, with $T_4 = \frac{\nabla\cdot\mathbf{b}}{b_z} + \frac{\mathbf{b}_H\cdot\nabla_H(D_A b_z)}{R_E D_A b_z^2}$, see above in eq.(B.41)

$$T_{5p}(z+\frac{1}{2}\Delta z) = b_z^2\left[\frac{1}{H\Delta z} + \frac{1}{2}\left(\frac{\nabla\cdot\mathbf{b}}{b_z} + \frac{\mathbf{b}_H\cdot\nabla_H(D_A b_z)}{R_E D_A b_z^2}(z+\frac{1}{2}\Delta z)\right)\right] \tag{B.42}$$

$$T_{5m}(z+\frac{1}{2}\Delta z) = b_z^2\left[\frac{1}{H\Delta z} - \frac{1}{2}\left(\frac{\nabla\cdot\mathbf{b}}{b_z} + \frac{\mathbf{b}_H\cdot\nabla_H(D_A b_z)}{R_E D_A b_z^2}(z+\frac{1}{2}\Delta z)\right)\right] \tag{B.43}$$

and stored in the variables *hdzpbz* and *hdzmdz* respectively.

The smoothing of $n(O^+)^{t_n-\Delta t}$ is finished with a longitudinal smoothing. See eq. (B.19) for the latitudinal smoothing

$$\begin{aligned} n(O^+)^{smo,t_n-\Delta t} = &n(O^+)^{smo\lambda,t_n-\Delta t} - f_{smo}[n(O^+)^{smo\lambda,t_n-\Delta t}(\phi+2\Delta\phi,\lambda)+ \\ &n(O^+)^{smo\lambda,t_n-\Delta t}(\phi-2\Delta\phi,\lambda) - 4(n(O^+)^{smo\lambda,t_n-\Delta t}(\phi+\Delta\phi,\lambda)+ \\ &n(O^+)^{smo\lambda,t_n-\Delta t}(\phi-\Delta\phi,\lambda)) + 6n(O^+)^{t_n-\Delta t}(\phi+\Delta\phi,\lambda)] \end{aligned} \tag{B.44}$$

with $f_{smo} = 0.003$. The smoothed number density is added to the explicit term $T_{2,explicit}$

$$T_{3,explicit} = T_{2,explicit} - \frac{n(O^+)^{smo,t_n-\Delta t}}{2\Delta t} \tag{B.45}$$

The tridiagonal solver need the equation in the following form:

$$\begin{aligned} P(k,i)n^{t+\Delta t}(k-1,i) + &Q(k,i)n^{t+\Delta t}(k,i)+ \\ &R(k,i)n^{t+\Delta t}(k+1,i) = T_{explicit}(k,i) \end{aligned} \tag{B.46}$$

with the height index k for $z+\frac{1}{2}\Delta z$, $k+1$ for $z+\frac{3}{2}\Delta z$, and $k-1$ for $z-\frac{1}{2}\Delta z$. The longitude index is denoted by i. Note that the equation is solved at each latitude λ with the index j.

The fourth and sixth term of the O^+ transport equation eq.(B.5) are treated implicit with the fourth term being

$$[(\mathbf{b}_h\cdot\nabla_h)Kb_z]\left[\left(\frac{1}{H}\frac{\partial}{\partial Z}(2T_p n) + \frac{mg}{k_B}n\right)\right]$$

and the sixth term

$$\left(b_z\frac{1}{H}\frac{\partial}{\partial Z} + \nabla\cdot\mathbf{b}\right)Kb_z\left(\frac{1}{H}\frac{\partial}{\partial Z}(2T_p n) + \frac{mg}{k_B}n\right)$$

$$P_1((z+\frac{1}{2}\Delta z),\phi) = T_{5m}(z+\frac{1}{2}\Delta z,\phi)D_A(z,\phi)S_m(z+\frac{1}{2}\Delta z,\phi) \tag{B.47}$$

$$\begin{aligned} Q_1((z+\frac{1}{2}\Delta z),\phi) = &-(T_{5p}(z+\frac{1}{2}\Delta z,\phi)D_A(z+\Delta z,\phi)S_m(z+\frac{3}{2}\Delta z,\phi)+ \\ &T_{5m}(z+\frac{1}{2}\Delta z,\phi)D_A(z,\phi)S_p(z+\frac{1}{2}\Delta z,\phi)) \end{aligned} \tag{B.48}$$

$$R_1((z+\frac{1}{2}\Delta z),\phi) = T_{5p}(z+\frac{1}{2}\Delta z,\phi)D_A(z+\Delta z,\phi)S_p(z+\frac{3}{2}\Delta z,\phi) \tag{B.49}$$

for the terms please see equations (B.33),(B.32), (B.38),(B.43),and (B.42).

The term $\mathbf{b} \cdot \mathbf{v}_n$ is determined

$$T_6(z + \frac{1}{2}\Delta z) = b_x u_n(z + \frac{1}{2}\Delta z) + b_y v_n(z + \frac{1}{2}\Delta z) + H(z + \frac{1}{2}\Delta z) b_z W(z + \frac{1}{2}\Delta z) \tag{B.50}$$

Note that the dimensionless vertical velocity W is on the interface level $z, z + \Delta z, ...$

Part of the seventh term in eq. (B.5) which is

$$(b_z \frac{1}{H} \frac{\partial}{\partial Z})(\mathbf{b} \cdot \mathbf{v}_n)$$

and the ninth term

$$B^2 \mathbf{v}_{ExB,z} \frac{1}{H} \frac{\partial}{\partial Z} \left(\frac{n}{B^2}\right)$$

are treated implicitly, leading to

$$P_2((z + \frac{1}{2}\Delta z), \phi) = P_1 + b_z \mathbf{b} \cdot \mathbf{v}_n((z + \frac{1}{2}\Delta z), \phi) + \mathbf{v}_{ExB,z}((z + \frac{3}{2}\Delta z), \phi) \frac{1}{2H(z + \frac{3}{2}\Delta z), \phi)\Delta z} \tag{B.51}$$

$$Q_2((z + \frac{1}{2}\Delta z), \phi) = Q_1 - \mathbf{v}_{ExB,z}((z + \frac{1}{2}\Delta z), \phi) \frac{6}{R_E} \tag{B.52}$$

$$R_2((z + \frac{1}{2}\Delta z), \phi) = R_1 - b_z mathbf b \cdot \mathbf{v}_n((z + \frac{3}{2}\Delta z), \phi) + \mathbf{v}_{ExB,z}((z + \frac{1}{2}\Delta z), \phi) \frac{1}{2H(z + \frac{1}{2}\Delta z), \phi)\Delta z} \tag{B.53}$$

The coefficients at the upper and lower boundary are set to

$$P_2^*((z_{bot} + \frac{1}{2}\Delta z), \phi) = P_2((z_{bot} + \frac{1}{2}\Delta z), \phi) + b_z[2\mathbf{b} \cdot \mathbf{v}_n((z_{bot} + \frac{1}{2}\Delta z), \phi) - \mathbf{b} \cdot \mathbf{v}_n((z_{bot} + \frac{3}{2}\Delta z), \phi)] + \mathbf{v}_{ExB,z}((z_{bot} + \frac{1}{2}\Delta z), \phi) \frac{1}{2H(z_{bot} + \frac{1}{2}\Delta z), \phi)\Delta z} \tag{B.54}$$

$$Q_2^*((z_{top} - \frac{1}{2}\Delta z), \phi) = Q_2((z_{top} - \frac{1}{2}\Delta z), \phi) - \mathbf{v}_{ExB,z}((z_{top} - \frac{1}{2}\Delta z), \phi) \frac{6}{R_E} \tag{B.55}$$

$$R_2^*((z_{top} - \frac{1}{2}\Delta z), \phi) = R_2(z_{top} - \frac{1}{2}\Delta z), \phi) - +??b_z[2\mathbf{b} \cdot \mathbf{v}_n((z_{top} - \frac{1}{2}\Delta z), \phi) - \mathbf{b} \cdot \mathbf{v}_n((z_{top} - \frac{3}{2}\Delta z), \phi)] + \mathbf{v}_{ExB,z}((z_{top} - \frac{1}{2}\Delta z), \phi) \frac{1}{2H(z_{top} - \frac{1}{2}\Delta z), \phi)\Delta z} \tag{B.56}$$

We add the other part of the seventh term in the transport equation (B.5)

$$(\nabla \cdot \mathbf{b})\,(\mathbf{b} \cdot v_n n)$$

and the time derivative of the number density of $n(O^+)$ to the Q–coefficient

$$Q_3((z + \frac{1}{2}\Delta z), \phi) = Q_2 - (b_z \nabla \cdot \mathbf{b}(\phi))(\mathbf{b} \cdot \mathbf{v}_n((z + \frac{1}{2}\Delta z), \phi)) - \frac{1}{2\Delta t} \tag{B.57}$$

The upper boundary condition is defined by

$$-b_z^2 D_a \left(T_p \frac{\partial}{H \partial Z} + \frac{mg}{R^*} \right) n = F^{O^+} \tag{B.58}$$

with F^{O^+} the flux of O^+ from and to the plasmasphere, which was defined in eq. (B.9) and (B.10).

$$B = - b_z^2 D_a(z_{top}) S_m(z_{top} + \frac{1}{2}\Delta z) \tag{B.59}$$

$$A = - b_z^2 D_a(z_{top}) S_p(z_{top} + \frac{1}{2}\Delta z) \tag{B.60}$$

with $S_m = 2T_p \frac{\partial}{H \partial Z} + \frac{mg}{R^*}$ from eq. (B.37) leading to

$$Q_3^*((z_{top} - \frac{1}{2}\Delta z), \phi) = Q_3((z_{top} - \frac{1}{2}\Delta z), \phi) + \frac{B}{A} R_2^*((z_{top} - \frac{1}{2}\Delta z), \phi) \tag{B.61}$$

and for the right hand side

$$\begin{aligned} T_{3,explicit}^*((z_{top} - \frac{1}{2}\Delta z), \phi) =& T_{3,explicit}((z_{top} - \frac{1}{2}\Delta z), \phi) - \\ & F^{O^+} R_2^*((z_{top} - \frac{1}{2}\Delta z), \phi) \frac{1}{A} \end{aligned} \tag{B.62}$$

The source and sink terms are calculated

$$\begin{aligned} n(XIO^+(^2P)) = & \frac{1}{2} \left(Q(O^+(^2P))(z) + Q(O^+(^2P))(z + \frac{1}{2}\Delta z) \right) \\ & \frac{1}{(k_{16} + k_{17}) n(N_2) + k_{18} n(O) + (k_{19} + k_{20}) N_e(z??) + k_{21} + k_{22}} \end{aligned} \tag{B.63}$$

$$\begin{aligned} n(XIO^+(^2D)) = & \frac{1}{2} \left(Q(O^+(^2D))(z) + Q(O^+(^2D))(z + \frac{1}{2}\Delta z) \right) + \\ & \frac{(k_{20} N_e(z??) + k_{22}) n(XIO^+(^2P))}{k_{23} n(N_2) + k_{24} n(O) + k_{26} n(O_2)} \end{aligned} \tag{B.64}$$

$$L^{O^+} = k_1 n(O_2) + k_2 n(N_2) + k_{10 n(N(^2D))} \tag{B.65}$$

The loss term L^{O^+} is added to the left hand side

$$Q_4((z + \frac{1}{2}\Delta z), \phi) = Q_3((z + \frac{1}{2}\Delta z), \phi) - L^{O^+} \tag{B.66}$$

The right hand side is updated by

$$\begin{aligned} T_{4,explicit}((z + \frac{1}{2}\Delta z), \phi) =& T_{3,explicit}((z + \frac{1}{2}\Delta z), \phi) - Q(O^+) - \\ & (k_{19} N_e(z) + k_{21}) n(XIO^+(^2P)) - \\ & (k_{25} N_e(z) + k_{27}) n(XIO^+(^2D)) - \\ & (k_{18} n(XIO^+(^2P)) + k_{24} n(XIO^+(^2D))) n(O) \end{aligned} \tag{B.67}$$

The lower boundary condition is specified by photochemical equilibrium $n = \frac{Q}{L}$ leading to

$$Q_4^*((z_{bot} + \frac{1}{2}\Delta z), \phi) = Q_4((z_{bot} + \frac{1}{2}\Delta z), \phi) - P_2((z_{bot} + \frac{1}{2}\Delta z), \phi) \tag{B.68}$$

$$\begin{aligned} T_{4,explicit}^*((z_{bot} + \frac{1}{2}\Delta z), \phi) = & T_{4,explicit}((z_{bot} + \frac{1}{2}\Delta z), \phi) - \\ & 2P_2((z_{bot} + \frac{1}{2}\Delta z), \phi) \frac{Q(O^+)}{1.5 L^{O^+}(z_{bot} + \frac{1}{2}\Delta z) - 0.5 L^{O^+}(z_{bot} + \frac{3}{2}\Delta z)} \end{aligned} \tag{B.69}$$

$$P_2^*((z_{bot} + \frac{1}{2}\Delta z), \phi) = 0 \tag{B.70}$$

Solving for the number density of O^+ at each latitude leads to the updated number densities $n(O^+)^{upd,t_n+\Delta t}$ at the midpoints. The calculated values for the number density of $n(O^+)^{upd,t+\Delta t}$ are smoothed by a Fast Fourier transformation leading to $n(O^+)^{upd,t+\Delta t}_{smo}$. All the wave numbers larger than a predefined value at each latitude are removed. The values of the number densities at the timestep t_n are also updated by using

$$n(O^+)^{upd,t} = \frac{1}{2}(1 - c_{smo})(n(O^+)^{t-\Delta t} + n(O^+)^{upd,t+\Delta t}_{smo}) + c_{smo} n(O^+)^{t_n} \tag{B.71}$$

with $c_{smo} = 0.95$ The upper boundary values are set to zero

$$n(O^+)^{upd,t_n}(z_{top} - \frac{1}{2}\Delta z) = 0 \tag{B.72}$$

$$n(O^+)^{upd,t_n}_{smo}(z_{top} - \frac{1}{2}\Delta z) = 0 \tag{B.73}$$

and the number density is set such that it has a minimum value of $1 \cdot 10^{-5}$.

$$n(O^+)^{upd,t_n}(z + \frac{1}{2}\Delta z) \geq 1 \cdot 10^{-5} \tag{B.74}$$

$$n(O^+)^{upd,t_n}_{smo}(z + \frac{1}{2}\Delta z) \geq 1 \cdot 10^{-5} \tag{B.75}$$

References

Akmaev, R. A. (2011), Whole atmosphere modeling: Connecting terrestrial and space weather, *Rev. Geophys.*, *49*, RG4004, doi:10.1029/2011RG000364.

Akmaev, R. A., T. J. Fuller-Rowell, F. Wu, J. M. Forbes, X. Zhang, A. F. Anghel, M. D. Iredell, S. Moorthi, and H. M. Juang (2008), Tidal variability in the lower thermosphere: Comparison of Whole Atmosphere Model (WAM) simulations with observations from TIMED, *Geophys. Res. Lett.*, *35*, L03810, doi:10.1029/2007GL032584.

Appleton, E. V. (1946), Two anomalies in the ionosphere, *Nature*, *157*, 691–693.

Basu, S., E. Kudeki, S. Basu, C. E. Valladares, E. J. Weber, H. P. Zengingonul, S. Bhattacharyya, R. Sheehan, J. W. Meriwether, M. A. Biondi, H. Kuenzler, and J. Espinoza (1996), Scintillations, plasma drifts, and neutral winds in the equatorial ionosphere after sunset, *Journal of Geophysical Research: Space Physics*, *101*, 26,795–26,809, doi:10.1029/96JA00760.

Bates, D. R. (1951), The temperature of the upper atmosphere, *, Proc. Phys. Soc., London, Sect. B*, *64*, 805.

Bilitza, D. (2001), International reference ionosphere 2000, *Radio Science*, *36*, 261–275, doi:10.1029/2000RS002432.

Chamberlin, P. C., T. N. Woods, and F. G. Eparvier (2007), Flare Irradiance Spectral Model (FISM): Daily component algorithms and results, *Space Weather*, *5*, 1895–1907, doi:10.1029/2007SW000316, s07005.

Chamberlin, P. C., T. N. Woods, and F. G. Eparvier (2008), Flare irradiance spectral model (fism): Flare component algorithms and results, *Space Weather*, *6*, doi:10.1029/2007SW000372, s05001.

Eccles, J. V. (2004), The effect of gravity and pressure in the electrodynamics of the low-latitude ionosphere, *Journal of Geophysical Research: Space Physics*, *109*, doi:10.1029/2003JA010023, a05304.

Emery, B. A., R. G. Roble, E. C. Ridley, A. D. Richmond, D. J. Knipp, G. Crowley, D. S. Evans, F. J. Rich, and S. Maeda (2012), Parameterization of the ion convection and the auroral oval in the ncar thermospheric general circulation models, *Tech. Rep. NCAR/TN-491+STR*, NCAR, Boulder, Colorado.

Eyring, V., ean François Lamarque, P. Hess, F. Arfeuille, K. Bowman, M. P. Chipperfiel, B. Duncan, A. Fiore, A. Gettelman, M. A. Giorgetta, C. Granier, M. Hegglin, D. Kinnison, M. Kunze, U. Langematz, B. Luo, R. Martin, K. Matthes, P. A. Newman, T. Peter, A. Robock, T. Ryerson, A. Saiz-Lopez, R. Salawitch, M. Schultz, T. G. Shepherd, D. Shindell, J. Staehelin, S. Tegtmeier, L. Thomason, S. Tilmes, J.-P. Vernier, D. W. Waugh, and P. J. Young (2013), Overview of IGAC/SPARC Chemistry-Climate Model Initiative (CCMI) community simulations in support of upcoming ozone and climate assessments, *SPARC Newsletter*, *40*, 48–66.

Fang, T.-W., R. Akmaev, T. Fuller-Rowell, F. Wu, N. Maruyama, and G. Millward (2013), Longitudinal and day-to-day variability in the ionosphere from lower atmosphere tidal forcing, *Geophysical Research Letters*, *40*, 2523–2528, doi:10.1002/grl.50550.

Fejer, B. G., E. R. de Paula, S. A. González, and R. F. Woodman (1991), Average vertical and zonal F region plasma drifts over jicamarca, *Journal of Geophysical Research: Space Physics*, *96*, 13,901–13,906, doi:10.1029/91JA01171.

Fejer, B. G., L. Scherliess, and E. R. de Paula (1999), Effects of the vertical plasma drift velocity on the generation and evolution of equatorial spread F, *J. Geophys. Res.*, *104*, 19,859–19,869.

Fejer, B. G., J. R. Souza, A. S. Santos, and A. E. Costa Pereira (2005), Climatology of F region zonal plasma drifts over Jicamarca, *J. Geophys. Res.*, *110*, A12310, doi:10.1029/2005JA011324.

Garcia, R. R., M. López-Puertas, B. Funke, D. R. Marsh, D. E. Kinnison, A. K. Smith, and F. González-Galindo (2014), On the distribution of CO2 and CO in the mesosphere and lower thermosphere, *Journal of Geophysical Research: Atmospheres*, *119*, 5700–

5718, doi:10.1002/2013JD021208.

Garcia, R. R., A. K. Smith, D. E. Kinnison, Álvaro de la Cámara, and D. J. Murphy (2017), Modification of the gravity wave parameterization in the whole atmosphere community climate model: Motivation and results, *Journal of the Atmospheric Sciences*, *74*, 275–291, doi:10.1175/JAS-D-16-0104.1.

Gentile, L. C., W. J. Burke, and F. J. Rich (2006), A climatology of equatorial plasma bubbles from DMSP 1989–2004, *Radio Science*, *41*, doi:10.1029/2005RS003340, rS5S21.

Goncharenko, L., J. Chau, H.-L. Liu, and A. J. Coster (2010a), Unexpected connections between the stratosphere and ionosphere, *Geophys. Res. Lett.*, *37*, L10101, doi:10.1029/2010GL043125.

Goncharenko, L., A. J. Coster, J. Chau, and C. Valladares (2010b), Impact of sudden stratospheric warmings on equatorial ionization anomaly, *J. Geophys. Res.*, *115*, A00G07, doi:10.1029/2010JA015400.

Hagan, M. E., A. Maute, R. G. Roble, A. D. Richmond, T. J. Immel, and S. L. England (2007), Connections between deep tropical clouds and the Earth's ionosphere, *Geophysical Research Letters*, *34*, doi:10.1029/2007GL030142.

Häusler, K., and H. Lühr (2009), Nonmigrating tidal signals in the upper thermospheric zonal wind at equatorial latitudes as observed by CHAMP, *Ann. Geophys.*, *27*, 2643–2652.

Heelis, R. A., J. K.Lowell, and R. W.Spiro (1982), A model of the high-latitude ionosphere convection pattern, *J. Geophys. Res.*, *87*, 6339–6345.

Huang, C.-S., and M. R. Hairston (2015), The postsunset vertical plasma drift and its effects on the generation of equatorial plasma bubbles observed by the c/nofs satellite, *Journal of Geophysical Research: Space Physics*, *120*, 2263–2275, doi:10.1002/2014JA020735, 2014JA020735.

Hurrell, J. W., M. M. Holland, P. R. Gent, S. Ghan, J. E. Kay, P. J. Kushner, J.-F. Lamarque, W. G. Large, D. Lawrence, K. Lindsay, W. H. Lipscomb, M. C. Long, N. Mahowald, D. R. Marsh, R. B. Neale, P. Rasch, S. Vavrus, M. Vertenstein, D. Bader, W. D. Collins, J. J. Hack, J. Kiehl, and S. Marshall (2013), The community earth system model: A framework for collaborative research, *Bulletin of the American Meteorological Society*, *94*, 1339–1360, doi:10.1175/BAMS-D-12-00121.1.

Immel, T. J., E. Sagawa, S. L. England, S. B. Henderson, M. E. Hagan, S. B. Mende, H. U. Frey, C. M. Swenson, and L. J. Paxton (2006), Control of equatorial ionospheric morphology by atmospheric tides, *Geophys. Res. Lett.*, *33*, doi:10.1029/2006GL026161.

Kaufmann, M., Y. Zhu, M. Ern, and M. Riese (2014), Global distribution of atomic oxygen in the mesopause region as derived from sciamachy O(1S) green line measurements, *Geophysical Research Letters*, *41*, 6274–6280, doi:10.1002/2014GL060574.

Kil, H., L. J. Paxton, and S.-J. Oh (2009), Global bubble distribution seen from ROCSAT-1 and its association with the evening prereversal enhancement, *Journal of Geophysical Research: Space Physics*, *114*, doi:10.1029/2008JA013672, a06307.

Kockarts, G., and W. Peetermans (1970), Atomic oxygen infrared emission in the earth's upper atmosphere, *Planet. Space Sci.*, *18*, 271.

Lauritzen, P. H., A. A. Mirin, J. Truesdale, K. Raeder, J. L. Anderson, J. Bacmeister, and R. B. Neale (2012), Implementation of new diffusion/filtering operators in the CAM-FV dynamical core, *The International Journal of High Performance Computing Applications*, *27 (1)*, 73–63, doi:10.1177/1094342011410088.

Lean, J., G. Rottman, J. Harder, and G. Kopp (2005), Sorce contributions to new understanding of global change and solar variability, *Solar Physics*, *230*, 27–53, doi:10.1007/s11207-005-1527-2.

Lei, J., J. P. Thayer, W. Wang, A. D. Richmond, R. Roble, X. Luan, X. Dou, X. Xue, and T. Li (2012), Simulations of the equatorial thermosphere anomaly: Field-aligned ion drag effect, *Journal of Geophysical Research: Space Physics*, *117*, doi:10.1029/2011JA017114, a01304.

Lin, S.-J. (1997), A finite-volume integration method for computing pressure gradient force in general vertical coordinates, *Quarterly Journal of the Royal Meteorological Society*, *123*, 1749–1762, doi:10.1002/qj.49712354214.

Lin, S.-J., and R. B. Rood (1996), Multidimensional flux-form semi-lagrangian transport schemes, *Monthly Weather Review*, *124*, 2046–2070, doi:10.1175/1520-0493(1996)124<2046:MFFSLT>2.0.CO;2.

Lin, S.-J., and R. B. Rood (1997), An explicit flux-form semi-lagrangian shallow-water model on the sphere, *Quarterly Journal of the Royal Meteorological Society*, *123*, 2477–2498, doi:10.1002/qj.49712354416.

Liu, H., H. Lühr, V. Henize, and W. Köhler (2005), Global distribution of the thermospheric total mass density derived from CHAMP, *Journal of Geophysical Research: Space Physics*, *110*, doi:10.1029/2004JA010741.

Liu, H., H. Lühr, and S. Watanabe (2007), Climatology of the equatorial thermospheric mass density anomaly, *Journal of Geophysical Research: Space Physics*, *112*, doi:10.1029/2006JA012199.

Liu, H.-L. (2016), Variability and predictability of the space environment as related to lower atmosphere forcing, *Space Weather*, *14*, 634–658, doi:10.1002/2016SW001450, 2016SW001450.

Liu, H.-L., and R. G. Roble (2002), A study of a self-generated stratospheric sudden warming and its mesospheric/lower thermospheric impacts using coupled TIME-GCM/CCM3, *J. Geophys. Res.*, *107*, doi:10.1029/2001JD001533.

Liu, H.-L., B. T. Foster, M. E. Hagan, J. M. McInerney, A. Maute, L. Qian, A. D. Richmond, R. G. Roble, S. C. Solomon, R. R. Garcia, D. Kinnison, D. R. Marsh, A. K. Smith, J. Richter, F. Sassi, and J. Oberheide (2010), Thermosphere extension of the Whole Atmosphere Community Climate Model, *J. Geophys. Res.*, *115*, A12302, doi:10.1029/2010JA015586.

Liu, H.-L., V. A. Yudin, and R. G. Roble (2013), Day-to-day ionospheric variability due to lower atmosphere perturbations, *Geophys. Res. Lett.*, doi:10.1002/grl.50125.

Liu, H.-L., J. M. McInerney, S. Santos, P. H. Lauritzen, M. A. Taylor, and N. M. Pedatella (2014), Gravity waves simulated by high-resolution Whole Atmosphere Community Climate Model, *Geophysical Research Letters*, *41*, 9106–9112, doi:10.1002/2014GL062468, 2014GL062468.

Liu, H.-L., et al. (2018), Development and validation of the Whole Atmosphere Community Climate Model with thermosphere and ionosphere extension (WACCM-X v. 2.0), *Journal of Advances in Modeling Earth Systems*, *10*, 381, doi:10.1002/2017MS001232.

Liu, J., W. Wang, A. Burns, X. Yue, S. Zhang, Y. Zhang, and C. Huang (2016a), Profiles of ionospheric storm-enhanced density during the 17 march 2015 great storm, *Journal of Geophysical Research: Space Physics*, *121*, 727–744, doi:10.1002/2015JA021832, 2015JA021832.

Liu, J., W. Wang, A. Burns, S. C. Solomon, S. Zhang, Y. Zhang, and C. Huang (2016b), Relative importance of horizontal and vertical transports to the formation of ionospheric storm-enhanced density and polar tongue of ionization, *Journal of Geophysical Research: Space Physics*, *121*, 8121–8133, doi:10.1002/2016JA022882, 2016JA022882.

Liu, J., H.-L. Liu, W. Wang, A. G. Burns, Q. Wu, Q. Gan, S. C. Solomon, D. R. Marsh, L. Qian, G. Lu, N. M. Pedatella, J. M. McInerney, J. M. R. III, and W. S. Schreiner (2017), First results from ionospheric extension of waccm-x during the deep solar minimum year 2008, *Journal of Geophysical Research: Space Physics*, in preparation.

Lu, G., L. Goncharenko, M. J. Nicolls, A. Maute, A. Coster, and L. J. Paxton (2012), Ionospheric and thermospheric variations associated with prompt penetration electric fields, *Journal of Geophysical Research: Space Physics*, *117*, doi:10.1029/2012JA017769, a08312.

Marsh, D. R., R. Garcia, D. Kinnison, B. Boville, F. Sassi, and S. Solomon (2007), Modeling the whole atmosphere response to solar cycle changes in radiative and geomagnetic forcing, *J. Geophys. Res.*, *112*, D23306, doi:10.1029/2006JD008306.

Marsh, D. R., M. J. Mills, D. E. Kinnison, J.-F. Lamarque, N. Calvo, and L. M. Polvani (2013), Climate Change from 1850 to 2005 Simulated in CESM1(WACCM), *Journal of Climate*, *26*, 7372–7391, doi:10.1175/JCLI-D-12-00558.1.

Maute, A. (2017), Thermosphere-ionosphere-electrodynamics general circulation model for the ionospheric connection explorer: Tiegcm-icon, *Space Science Reviews*, *212*, 523–551, doi:10.1007/s11214-017-0330-3.

Maute, A., A. D. Richmond, and R. G. Roble (2012), Sources of low-latitude ionospheric e × b drifts and their variability, *Journal of Geophysical Research: Space Physics*, *117*, doi:10.1029/2011JA017502, a06312.

Miyoshi, Y., H. Fujiwara, H. Jin, H. Shinagawa, H. Liu, and K. Terada (2011), Model study on the formation of the equatorial mass density anomaly in the thermosphere, *Journal of Geophysical Research: Space Physics*, *116*, doi:10.1029/2010JA016315.

Miyoshi, Y., H. Fujiwara, H. Jin, H. Shinagawa, and H. Liu (2012), Numerical simulation of the equatorial wind jet in the thermosphere, *Journal of Geophysical Research: Space Physics*, *117*, doi:10.1029/2011JA017373.

Mlynczak, M. G., L. A. Hunt, J. C. Mast, B. Thomas Marshall, J. M. Russell, A. K. Smith, D. E. Siskind, J.-H. Yee, C. J. Mertens, F. Javier Martin-Torres, R. Earl Thompson, D. P. Drob, and L. L. Gordley (2013), Atomic oxygen in the mesosphere and lower thermosphere derived from saber: Algorithm theoretical basis and measurement uncertainty, *Journal of Geophysical Research: Atmospheres*, *118*, 5724–5735, doi:10.1002/jgrd.50401.

Neale, R. B., J. H. Richter, S. Park, P. H. Lauritzen, S. J. Vavrus, P. J. Rasch, and M. Zhang (2013), The mean climate of the Community Atmosphere Model (CAM4) in forced SST and fully coupled experiments, *J. Climate*, *26*, 5150–5168, doi:10.1175/JCLI-D-12-00236.1.

Oberheide, J., J. M. Forbes, K. Häusler, Q. Wu, and S. L. Bruinsma (2009), Tropospheric tides from 80 to 400 km: Propagation, interannual variability, and solar cycle effects, *J. Geophys. Res.*, *114*, D00I05, doi:10.1029/2009JD012388.

Pedatella, N. M., H.-L. Liu, A. D. Richmond, A. Maute, and T.-W. Fang (2012), Simulations of solar and lunar tidal variability in the mesosphere and lower thermosphere during sudden stratosphere warmings and their influence on the low-latitude ionosphere, *J. Geophys. Res.*, *117*, A08326, doi:10.1029/2012JA017858.

Pedatella, N. M., K. Raeder, J. L. Anderson, and H.-L. Liu (2014), Ensemble data assimilation in the whole atmosphere community climate model, *J. Geophys. Res.*, *119*, 9793–9809, doi:10.1002/2014JD021776.

Picone, J. M., A. E. Hedin, D. P. Drob, and A. C. Aikin (2002), NRLMSISE-00 empirical model of the atmosphere: Statistical comparisons and scientific issues, *J. Geophys. Res.*, *107*, 1468, doi:doi:10.1029/2002JA009430.

Qian, L., and S. C. Solomon (2012), Thermospheric density: An overview of temporal and spatial variations, *Space Science Reviews*, *168*, 147–173, doi:10.1007/s11214-011-9810-z.

Qian, L. Y., S. C. Solomon, and T. J. Kane (2009), Seasonal variation of thermospheric density and composition, *J. Geophys. Res.*, *114*, A01312, doi:10.1029/2008JA013643.

Qian, L. Y., A. G. Burns, P. C. Chamberlin, and S. C. Solomon (2010), Flare location on the solar disk: The effect on thermosphere and ionosphere response, *J. Geophys. Res.*, *115*, A09311, doi:10.1029/2009JA015225.

Qian, L. Y., A. G. Burns, B. A. Emery, B. Foster, G. Lu, A. Maute, A. D. Richmond, R. G. Roble, S. C. Solomon, and W. Wang (2014), The NCAR TIE-GCM: A community model of the coupled thermosphere/ionosphere system, Modeling the Ionosphere-Thermosphere System, in *Modeling the Ionosphere and Thermosphere System*, edited by J. Huba, R. Schunk, and G. Khazanov, Geophysical Monograph Series, chap. 7, p. 73, Wiley, Chichester, UK, doi:10.1002/9781118704417.ch7.

Rees, M. H., and R. G. Roble (1975), Observations and theory of the formation of stable auroral red arcs, *Rev. Geophys. Space Phys.*, *13*, 201–242.

Richmond, A. D. (1995), Ionospheric electrodynamics using magnetic apex coordinates, *J. Geomagn. Geoelectr.*, *47*, 191–212.

Richmond, A. D., and Y. Kamide (1988), Mapping electrodynamic features of the high-latitude ionosphere from localized observations: Technique, *Journal of Geophysical Research: Space Physics*, *93*, 5741–5759, doi:10.1029/JA093iA06p05741.

Richmond, A. D., and A. Maute (2014), Ionospheric electrodynamics modeling, in *Modeling the Ionosphere and Thermosphere System*, edited by J. Huba, R. Schunk, and G. Khazanov, Geophysical Monograph Series, chap. 6, pp. 57–71, Wiley, Chichester, UK, doi:10.1002/9781118704417.ch6.

Richmond, A. D., E. C. Ridley, and R. G. Roble (1992), A thermosphere/ionosphere general circulation model with coupled electrodynamics, *Geophys. Res. Lett.*, *19*, 601–604.

Richmond, A. D., T.-W. Fang, and A. Maute (2015), Electrodynamics of the equatorial evening ionosphere: 1. importance of winds in different regions, *Journal of Geophysical Research: Space Physics*, *120*, 2118–2132, doi:10.1002/2014JA020934, 2014JA020934.

Richter, J. H., , F. Sassi, and R. R. Garcia (2010), Toward a physically based gravity wave source parameterization in a general circulation model, *J. Atmos. Sci.*, *67*, 136–156, doi:10.1175/2009JAS3112.1.

Rishbeth, H. (2002), Whatever happened to superrotation?, *Journal of Atmospheric and Solar-Terrestrial Physics*, *64*, 1351 – 1360.

Roble, R., and J. Hastings (1977), Thermal response properties of the earth's ionospheric plasma, *Planetary and Space Science*, *25*, 217 – 231, doi:10.1016/0032-0633(77)90133-7.

Roble, R. G. (1995), Energetics of the mesosphere and thermosphere, in *The Upper Mesosphere and Lower Thermosphere: A Review of Experiment and Theory*, edited by R. M. Johnson and T. L. Killeen, no. 87 in Geophysical Monograph Series, p. 356, Americal Geophysical Union.

Roble, R. G., and E. C. Ridley (1987), An auroral model for the ncar thermosphere general circulation model (TGCM), *Annales. Geophysicae*, *5A*, 369–382.

Roble, R. G., and E. C. Ridley (1994), A thermosphere-ionosphere-mesosphere-electrodynamics general circulation model (TIME-GCM): Equinox solar cycle minimum simulations (30-500 km), *Geophys. Res. Lett.*, *21*, 417–420.

Roble, R. G., E. C. Ridley, A. D. Richmond, and R. E. Dickinson (1988), A coupled thermosphere/ionosphere general circulation model, *Geophys. Res. Lett.*, *15*, 1325–1328.

Ruan, H., J. Lei, X. Dou, W. Wan, and Y. Liu (2014), Midnight density maximum in the thermosphere from the champ observations, *Journal of Geophysical Research: Space Physics*, *119*(5), 3741–3746, doi:10.1002/2013JA019566, 2013JA019566.

Russell, J. P., W. E. Ward, R. P. Lowe, R. G. Roble, G. G. Shepherd, and B. Solheim (2005), Atomic oxygen profiles (80 to 115 km) derived from wind imaging interferometer/upper atmospheric research satellite measurements of the hydroxyl and greenline airglow: Local time–latitude dependence, *Journal of Geophysical Research: Atmospheres*, *110*, doi:10.1029/2004JD005570, d15305.

Sander, S. P., J. Abbatt, J. R. Barker, J. B. Burkholder, R. R. Friedl, D. M. Golden, R. E. Huie, C. E. Kolb, M. J. Kurylo, G. K. Moortgat, V. L. Orkin, and P. H. Wine (2011), Chemical kinetics and photochemical data for use in atmospheric studies, evaluation no. 17, *JPL Publication 10-6*, NASA-JPL, Pasadena, California.

Scherliess, L., and B. G. Fejer (1999), Radar and satellite global equatorial f region vertical drift model, *J. Geophys. Res.*, *104*, 6829–6842.

Schunk, R. W., and A. F. Nagy (2009), *Ionospheres, Physics, Plasma Physics, and Chemistry (2nd ed.)*, 628 pp., Cambridge University Press, Cambridge, UK.

Sharma, R. D., P. P. Wintersteiner, and K. S. Kalogerakis (2015), A new mechanism for oh vibrational relaxation leading to enhanced co2 emissions in the nocturnal mesosphere, *Geophysical Research Letters*, *42*, 4639–4647, doi:10.1002/2015GL063724.

Sheese, P. E., I. C. McDade, R. L. Gattinger, and E. J. Llewellyn (2011), Atomic oxygen densities retrieved from optical spectrograph and infrared imaging system observations

of o2 a-band airglow emission in the mesosphere and lower thermosphere, *Journal of Geophysical Research: Atmospheres*, *116*, doi:10.1029/2010JD014640, d01303.

Smith, A. K., D. R. Marsh, M. G. Mlynczak, and J. C. Mast (2010), Temporal variations of atomic oxygen in the upper mesosphere from saber, *Journal of Geophysical Research: Atmospheres*, *115*, doi:10.1029/2009JD013434, d18309.

Smithtro, C. G., and S. C. Solomon (2008), An improved parameterization of thermal electron heating by photoelectrons, with application to an x17 flare, *Journal of Geophysical Research: Space Physics*, *113*, doi:10.1029/2008JA013077, a08307.

Solomon, S., D. Kinnison, J. Bandoro, and R. Garcia (2015a), Simulation of polar ozone depletion: An update, *J. Geophys. Res.*, *120*, doi:10.1002/2015JD023365.

Solomon, S. C. (2017), Global modeling of thermospheric airglow in the far ultraviolet, *Journal of Geophysical Research: Space Physics*, *122*, 7834–7848, doi:10.1002/2017JA024314.

Solomon, S. C., and L. Qian (2005), Solar extreme-ultraviolet irradiance for general circulation models, *J. Geophys. Res.*, *110*, A10306, doi:10.1029/2005JA011160.

Solomon, S. C., A. G. Burns, B. A. Emery, M. G. Mlynczak, L. Qian, W. Wang, D. R. Weimer, and M. Wiltberger (2012), Modeling studies of the impact of high-speed streams and co-rotating interaction regions on the thermosphere-ionosphere, *J. Geophys. Res.*, *117*, doi:10.1029/2011JA017417.

Solomon, S. C., L. Qian, and R. G. Roble (2015b), New 3d simulations of climate change in the thermosphere, *J. Geophys. Res.*, *120*, doi:10.1002/2014JA020886.

Swartz, W. E., and J. S. Nisbet (1972), Revised calculations of f region ambient electron heating by photoelectrons, *Journal of Geophysical Research*, *77*, 6259–6261, doi:10.1029/JA077i031p06259.

Thébault, E., C. C. Finlay, C. D. Beggan, P. Alken, J. Aubert, O. Barrois, F. Bertrand, T. Bondar, A. Boness, L. Brocco, E. Canet, A. Chambodut, A. Chulliat, P. Coïsson, F. Civet, A. Du, A. Fournier, I. Fratter, N. Gillet, B. Hamilton, M. Hamoudi, G. Hulot, T. Jager, M. Korte, W. Kuang, X. Lalanne, B. Langlais, J.-M. Léger, V. Lesur, F. J. Lowes, S. Macmillan, M. Mandea, C. Manoj, S. Maus, N. Olsen, V. Petrov, V. Ridley, M. Rother, T. J. Sabaka, D. Saturnino, R. Schachtschneider, O. Sirol, A. Tangborn, A. Thomson, L. Tøffner-Clausen, P. Vigneron, I. Wardinski, and T. Zvereva (2015), International Geomagnetic Reference Field: the 12th generation, *Earth, Planets and Space*, *67*, 79, doi:10.1186/s40623-015-0228-9.

Titheridge, J. (2003), Ionisation below the night F2 layer–a global model, *Journal of Atmospheric and Solar-Terrestrial Physics*, *65*, 1035–1052, doi:http://dx.doi.org/10.1016/S1364-6826(03)00136-6.

Wang, W. (1998), *A Thermosphere-Ionosphere Nested Grid (TING) Model*, 305 pp., Ph.D. Dissertation, The University of Michigan, Ann Arbor, MI.

Wang, W., J. Lei, A. G. Burns, S. C. Solomon, M. Wiltberger, J. Xu, Y. Zhang, L. Paxton, and A. Coster (2010), Ionospheric response to the initial phase of geomagnetic storms: Common features, *Journal of Geophysical Research: Space Physics*, *115*, doi:10.1029/2009JA014461, a07321.

Weimer, D. R. (2005), Improved ionospheric electrodynamic models and application to calculating joule heating rates, *J. Geophys. Res.*, *110*, A05306.

Wu, Q., D. A. Ortland, S. C. Solomon, W. R. Skinner, and R. J. Niciejewski (2011), Global distribution, seasonal, and inter-annual variations of mesospheric semidiurnal tide observed by TIMED TIDI, *J. Atmos. Solar Terr. Phys.*, *73*, 2482–2502, doi:10.1016/j.jastp.2011.08.007.

Zhang, Y., and L. Paxton (2008), An empirical kp-dependent global auroral model based on TIMED/GUVI FUV data, *Journal of Atmospheric and Solar-Terrestrial Physics*, *70*, 1231 – 1242, doi:http://dx.doi.org/10.1016/j.jastp.2008.03.008.